A&A, 711, A33 (2026)
https://doi.org/10.1051/0004-6361/202554577
© The Authors 2026

Astronomy & Astrophysics
Special issue

Euclid Quick Data Release (Q1)

Euclid Quick Data Release (Q1)

XXXIII. The first catalogue of strong-lensing galaxy clusters

Euclid Collaboration: P. Bergamini[1,2,⋆], M. Meneghetti[2,3], A. Acebron[4], B. Clément[5,6], M. Bolzonella[2], C. Grillo[1,7], P. Rosati[8,2], D. Abriola[1], J. A. Acevedo Barroso[5], G. Angora[9,8], L. Bazzanini[8,2], R. Cabanac[10], B. C. Nagam[11,12], A. R. Cooray[13], G. Despali[14,2,3], G. Di Rosa[8], J. M. Diego[4], M. Fogliardi[8], A. Galan[15,16], R. Gavazzi[17,18], G. Granata[19], N. B. Hogg[20], K. Jahnke[21], L. Leuzzi[14,2], T. Li[19], M. Lombardi[1], G. Mahler[22,23,24], A. Manjón-García[25], R. B. Metcalf[14,2], M. Oguri[26,27], C. Olave[28], J. M. Palencia[4], J. Richard[29], K. Rojas[30,19], L. R. Ecker[31,32], C. Scarlata[11], M. Schirmer[21], S. Schuldt[1,7], D. Sluse[22], G. P. Smith[33,34], C. Tortora[9], G. Vernardos[35,36], G. L. Walth[37], J. Wilde[38], Y. Xie[5,39], M. Zumalacarregui[40], N. Aghanim[41], B. Altieri[42], A. Amara[43], L. Amendola[44], S. Andreon[45], N. Auricchio[2], H. Aussel[46], C. Baccigalupi[47,48,49,50], M. Baldi[28,2,3], A. Balestra[51], S. Bardelli[2], A. Basset[52], P. Battaglia[2], R. Bender[32,31], A. Biviano[48,47], A. Bonchi[53], D. Bonino[54], E. Branchini[55,56,45], M. Brescia[57,9], J. Brinchmann[58,59], A. Caillat[17], S. Camera[60,61,54], G. Cañas-Herrera[62,63,64], V. Capobianco[54], C. Carbone[7], J. Carretero[65,66], S. Casas[67], F. J. Castander[68,69], M. Castellano[70], G. Castignani[2], S. Cavuoti[9,71], K. C. Chambers[72], A. Cimatti[73], C. Colodro-Conde[74], G. Congedo[75], C. J. Conselice[76], L. Conversi[77,42], Y. Copin[78], F. Courbin[38,79], H. M. Courtois[80], M. Cropper[81], A. Da Silva[82,83], H. Degaudenzi[84], G. De Lucia[48], A. M. Di Giorgio[85], C. Dolding[81], H. Dole[41], F. Dubath[84], X. Dupac[42], S. Dusini[86], A. Ealet[78], S. Escoffier[87], M. Fabricius[32,31], M. Farina[85], R. Farinelli[2], F. Faustini[70,53], S. Ferriol[78], F. Finelli[2,88], P. Fosalba[69,68], S. Fotopoulou[89], M. Frailis[48], E. Franceschi[2], M. Fumana[7], S. Galeotta[48], K. George[31], B. Gillis[75], C. Giocoli[2,3], P. Gómez-Alvarez[90,42], J. Gracia-Carpio[32], B. R. Granett[45], A. Grazian[51], F. Grupp[32,31], L. Guzzo[1,45,91], S. V. H. Haugan[92], H. Hoekstra[64], W. Holmes[93], F. Hormuth[94], A. Hornstrup[95,96], P. Hudelot[18], M. Jhabvala[97], B. Joachimi[98], E. Keihänen[99], S. Kermiche[87], A. Kiessling[93], M. Kilbinger[46], R. Kohley[42], B. Kubik[78], K. Kuijken[64], M. Kümmel[31], M. Kunz[100], H. Kurki-Suonio[101,102], O. Lahav[98], R. Laureijs[12], Q. Le Boulc'h[103], A. M. C. Le Brun[104], D. Le Mignant[17], P. Liebing[81], S. Ligori[54], P. B. Lilje[92], V. Lindholm[101,102], I. Lloro[105], G. Mainetti[103], D. Maino[1,7,91], E. Maiorano[2], O. Mansutti[48], S. Marcin[106], O. Marggraf[107], M. Martinelli[70,108], N. Martinet[17], F. Marulli[14,2,3], R. Massey[24], S. Maurogordato[109], E. Medinaceli[2], S. Mei[110,111], M. Melchior[30], Y. Mellier[112,18], E. Merlin[70], G. Meylan[5], A. Mora[113], M. Moresco[14,2], L. Moscardini[14,2,3], S. Mourre[109,114], R. Nakajima[107], C. Neissner[115,66], R. C. Nichol[43], S.-M. Niemi[62], J. W. Nightingale[116], C. Padilla[115], S. Paltani[84], F. Pasian[48], K. Pedersen[117], W. J. Percival[118,119,120], V. Pettorino[62], S. Pires[46], G. Polenta[53], M. Poncet[52], L. A. Popa[121], L. Pozzetti[2], F. Raison[32], R. Rebolo[74,122,123], A. Renzi[124,86], J. Rhodes[93], G. Riccio[9], E. Romelli[48], M. Roncarelli[2], B. Rusholme[37], R. Saglia[31,32], Z. Sakr[44,10,125], D. Sapone[126], B. Sartoris[31,48], J. A. Schewtschenko[75], P. Schneider[107], A. Secroun[87], G. Seidel[21], M. Seiffert[93], S. Serrano[69,127,68], P. Simon[107], C. Sirignano[124,86], G. Sirri[3], A. Spurio Mancini[128], L. Stanco[86], J. Steinwagner[32], P. Tallada-Crespí[65,66], A. N. Taylor[75], H. I. Teplitz[129], I. Tereno[82,130], N. Tessore[98], S. Toft[131,132], R. Toledo-Moreo[133], F. Torradeflot[66,65], A. Tsyganov[134], I. Tutusaus[10], E. A. Valentijn[12], L. Valenziano[2,88], J. Valiviita[101,102], T. Vassallo[31,48], G. Verdoes Kleijn[12], A. Veropalumbo[45,56,55], Y. Wang[129], J. Weller[31,32], A. Zacchei[48,47], G. Zamorani[2], F. M. Zerbi[45], E. Zucca[2], V. Allevato[9], M. Ballardini[8,135,2], E. Bozzo[84], C. Burigana[136,88], A. Cappi[2,109], P. Casenove[52], D. Di Ferdinando[3], J. A. Escartin Vigo[32], L. Gabarra[137], J. Martín-Fleitas[113], S. Matthew[75], M. Maturi[44,138], N. Mauri[73,3], A. A. Nucita[139,140,141], A. Pezzotta[142,32], M. Pöntinen[101], C. Porciani[107], I. Risso[143], V. Scottez[112,144], M. Sereno[2,3], M. Tenti[3], M. Viel[47,48,50,49,145],

⋆ Corresponding author: pietro.bergamini@inaf.it

Open Access article, published by EDP Sciences, under the terms of the Creative Commons Attribution License (https://creativecommons.org/licenses/by/4.0), which permits unrestricted use, distribution, and reproduction in any medium, provided the original work is properly cited.
This article is published in open access under the Subscribe to Open model. Subscribe to A&A to support open access publication.

M. Wiesmann[92], Y. Akrami[146,147], I. T. Andika[15,16], S. Anselmi[86,124,148], M. Archidiacono[1,91], F. Atrio-Barandela[149], C. Benoist[109], K. Benson[81], D. Bertacca[124,51,86], M. Bethermin[150], A. Blanchard[10], L. Blot[151,148], H. Böhringer[32,152,153], S. Borgani[154,47,48,49,145], M. L. Brown[76], S. Bruton[155], A. Calabro[70], B. Camacho Quevedo[69,68], F. Caro[70], C. S. Carvalho[130], T. Castro[48,49,47,145], F. Cogato[14,2], O. Cucciati[2], S. Davini[56], F. De Paolis[139,140,141], G. Desprez[12], A. Díaz-Sánchez[25], J. J. Diaz[156], S. Di Domizio[55,56], P.-A. Duc[150], A. Enia[28,2], Y. Fang[31], A. G. Ferrari[3], P. G. Ferreira[137], A. Finoguenov[101], A. Fontana[70], A. Franco[140,139,141], K. Ganga[110], J. García-Bellido[146], T. Gasparetto[48], V. Gautard[157], E. Gaztanaga[68,69,19], F. Giacomini[3], F. Gianotti[2], A. H. Gonzalez[158], G. Gozaliasl[159,101], M. Guidi[28,2], C. M. Gutierrez[156], A. Hall[75], W. G. Hartley[84], C. Hernández-Monteagudo[123,74], H. Hildebrandt[160], J. Hjorth[117], O. Ilbert[17], M. Jauzac[23,24,161,162], J. J. E. Kajava[163,164], Y. Kang[84], V. Kansal[165,166], D. Karagiannis[8,167], K. Kiiveri[99], C. C. Kirkpatrick[99], S. Kruk[42], J. Le Graet[87], L. Legrand[168,169], M. Lembo[8,135], F. Lepori[170], G. Leroy[23,24], G. F. Lesci[14,2], J. Lesgourgues[67], T. I. Liaudat[171], S. J. Liu[85], A. Loureiro[172,173], J. Macias-Perez[174], G. Maggio[48], M. Magliocchetti[85], F. Mannucci[175], R. Maoli[176,70], C. J. A. P. Martins[177,58], L. Maurin[41], M. Migliaccio[178,179], M. Miluzio[42,180], P. Monaco[154,48,49,47], C. Moretti[50,145,48,47,49], G. Morgante[2], C. Murray[110], S. Nadathur[19], K. Naidoo[19], A. Navarro-Alsina[107], S. Nesseris[146], F. Passalacqua[124,86], K. Paterson[21], L. Patrizii[3], A. Pisani[87,181], D. Potter[170], S. Quai[14,2], M. Radovich[51], P. Reimberg[112], P.-F. Rocci[41], G. Rodighiero[124,51], S. Sacquegna[139,140,141], M. Sahlén[182], D. B. Sanders[72], E. Sarpa[50,145,49], A. Schneider[170], M. Schultheis[109], D. Sciotti[70,108], E. Sellentin[183,64], F. Shankar[184], L. C. Smith[185], S. A. Stanford[186], K. Tanidis[137], C. Tao[87], G. Testera[56], R. Teyssier[181], S. Tosi[55,56,45], A. Troja[124,86], M. Tucci[84], C. Valieri[3], A. Venhola[187], D. Vergani[2], G. Verza[188], P. Vielzeuf[87], N. A. Walton[185], E. Soubrie[41], and D. Scott[189]

(Affiliations can be found after the references)

Received 17 March 2025 / Accepted 15 September 2025

ABSTRACT

We present the first catalogue of strong-lensing galaxy clusters identified in the Euclid Quick Release 1 observations (covering 63.1 deg^2). This catalogue is the result of the visual inspection of 1260 *Euclid* image cutouts of previously identified galaxy clusters. Each galaxy cluster was assigned a lensing score, $\mathcal{P}_{\rm lens}$, derived from the aggregated votes of multiple visual inspectors, the majority of whom possess extensive expertise in strong gravitational lensing. Votes were assigned based on the assessed credibility and plausibility of the identified strong-lensing features. Specifically, we identified 83 gravitational lenses with $\mathcal{P}_{\rm lens} > 0.5$, of which 14 have $\mathcal{P}_{\rm lens} = 1$ and clearly exhibit secure strong-lensing features, such as giant tangential and radial arcs, and multiple images. Considering the measured number density of lensing galaxy clusters, approximately 0.3 deg^{-2} for $\mathcal{P}_{\rm lens} > 0.9$, we predict that *Euclid* will likely observe more than 4500 strong-lensing clusters over the course of the mission. Notably, only three of the identified cluster-scale lenses had previously been observed from space. Thus, *Euclid* has provided the first high-resolution imaging for the remaining 80 strong-lensing galaxy cluster candidates, including those with the highest scores. The identified strong-lensing features will be used to train deep-learning models to automatically identify gravitational arcs and multiple images in the *Euclid* observations. This study confirms the great potential of *Euclid* for finding new strong-lensing clusters, enabling exciting new discoveries on the nature of dark matter and dark energy and the study of the high-redshift Universe.

Key words. gravitational lensing: strong – galaxies: clusters: general – cosmology: observations – dark matter

1. Introduction

Gravitational lensing in galaxy clusters is widely recognised as a powerful tool for determining their total mass distribution, including baryonic and dark components, across scales ranging from several kiloparsecs to megaparsecs. This can be achieved through strong lensing (e.g. Grillo et al. 2015; Mahler et al. 2018; Bergamini et al. 2023; Diego et al. 2023; Furtak et al. 2023; Acebron et al. 2024), weak lensing (e.g. Medezinski et al. 2016; Umetsu et al. 2020), or combined analyses (e.g. Jauzac et al. 2016; Liesenborgs et al. 2020; Niemiec et al. 2023). These methods also enable the measurement of key cosmological parameters that govern cosmic geometry and the expansion rate (e.g. Jullo et al. 2010; Caminha et al. 2016, 2022; Magaña et al. 2018; Grillo et al. 2024), as well as the detailed study of the intrinsic properties of background lensed galaxies (e.g. Coe et al. 2013; Bouwens et al. 2014; Hashimoto et al. 2018; Meštrić et al. 2022; Vanzella et al. 2024).

Strong-lensing galaxy clusters are relatively rare (Oguri 2010), underscoring the critical role of wide-field surveys in building statistical samples. High-resolution optical and near-infrared imaging is particularly effective for identifying strong-lensing features with precision and reliability. However, such observations are typically constrained by small fields of view, often limited to a few arcminutes. This limitation has likely contributed to the relatively small number of studies leveraging high-resolution space-based observations to significantly expand samples of strong-lensing galaxy clusters (e.g. the MACS, beyond-MACS, RELICS, or SGAS-HST surveys, Ebeling et al. 2001, 2025; Coe et al. 2019; Sharon et al. 2020).

Owing to its unique combination of high-resolution and wide-area survey capabilities, *Euclid* is poised to revolutionise the field of strong lensing by galaxy clusters. Although *Euclid* will ultimately survey approximately 14 000 deg^2 of the sky in the optical and near-infrared (Euclid Collaboration: Mellier et al. 2025), the Euclid Quick Release Q1 (2025) already holds immense potential to contribute significantly to the scientific goals

outlined above. The Q1 dataset (Euclid Collaboration: Aussel et al. 2026; Euclid Collaboration: McCracken et al. 2026; Euclid Collaboration: Polenta et al. 2026; Euclid Collaboration: Romelli et al. 2026; Euclid Collaboration: Tucci et al. 2025; Euclid Collaboration: Copin et al. 2026; Euclid Collaboration: Le Brun et al. 2026) encompasses the three Euclid Deep Fields (EDFs), covering a total area of 63.1 deg^2 to the depth of the Euclid Wide Survey (EWS, Euclid Collaboration: Scaramella et al. 2022).

This potential is exemplified by the first results from *Euclid*'s Early Release Observations (Cuillandre et al. 2025) of two lensing galaxy clusters, Abell 2390 and Abell 2764 (Atek et al. 2025; Diego et al. 2026). These studies highlight *Euclid* ability to map the total mass distribution of such systems and identify candidate high-redshift ($z > 6$) dropout sources (see also Weaver et al. 2025). By broadening the discovery window and providing a platform for validating detection and analysis techniques, the Q1 release marks an important milestone in the mission's scientific journey.

This work investigates *Euclid*'s potential to uncover strong-lensing galaxy clusters. In particular, we produce the first catalogue of cluster-scale strong-lensing features and giant arcs observed by the *Euclid* telescope. This effort is essential to generate efficient training sets for sophisticated machine learning algorithms to be applied to the *Euclid* imaging data in Data Release 1 (DR1) and beyond (e.g. Euclid Collaboration: Bazzanini et al. 2026), where analyses based solely on visual inspections will be extremely challenging. To achieve these goals, we perform the first systematic visual inspection of the Q1 data, covering an effective area of ∼4.4 deg^2 (about 10% of Q1), and study the prevalence of strong-lensing clusters in an optically selected sample of galaxy clusters based on richness. Given the large areas to be examined, we exploit the tool `galaxyvote` developed by Meneghetti et al. (in prep.), which enables inspectors to efficiently review large samples of images, with functionalities equally well suited to search for galaxy-, group-, and cluster-scale lenses.

This paper is organised as follows. In Sect. 2, we briefly describe the *Euclid* imaging data and the creation of colour images of candidate lensing galaxy clusters. Section 3 provides an overview of the galaxy cluster catalogue, the properties and capabilities of the newly developed tool `galaxyvote`, and the adopted methodology for the visual inspection. Our results are presented and discussed in Sect. 4. Finally, we draw our conclusions in Sect. 5. Throughout the paper, we assume a flat ΛCDM cosmology with $H_0 = 70$ kms^{-1} Mpc^{-1} and a matter density $\Omega_m = 0.3$. Magnitudes are given in the AB system (Oke 1974), and statistical uncertainties correspond to 68% confidence levels.

2. Data and colour image generation

All results presented in this work are based on the *Euclid* observations in the I_E, Y_E, J_E, and H_E photometric filters (Euclid Collaboration: Cropper et al. 2025; Euclid Collaboration: Jahnke et al. 2025) from the Q1 data release, which covers a total sky area of approximately 63.1 deg^2, corresponding to the combined areas of the three EDFs (see Fig. 1, EDF-N 22.9 deg^2, EDF-F 12.1 deg^2, and EDF-S 28.1 deg^2), but observed at the depth of the EWS. For the I_E filter, this corresponds to a signal-to-noise ratio (S/N) ≥ 10 for extended sources with a full width at half maxi-

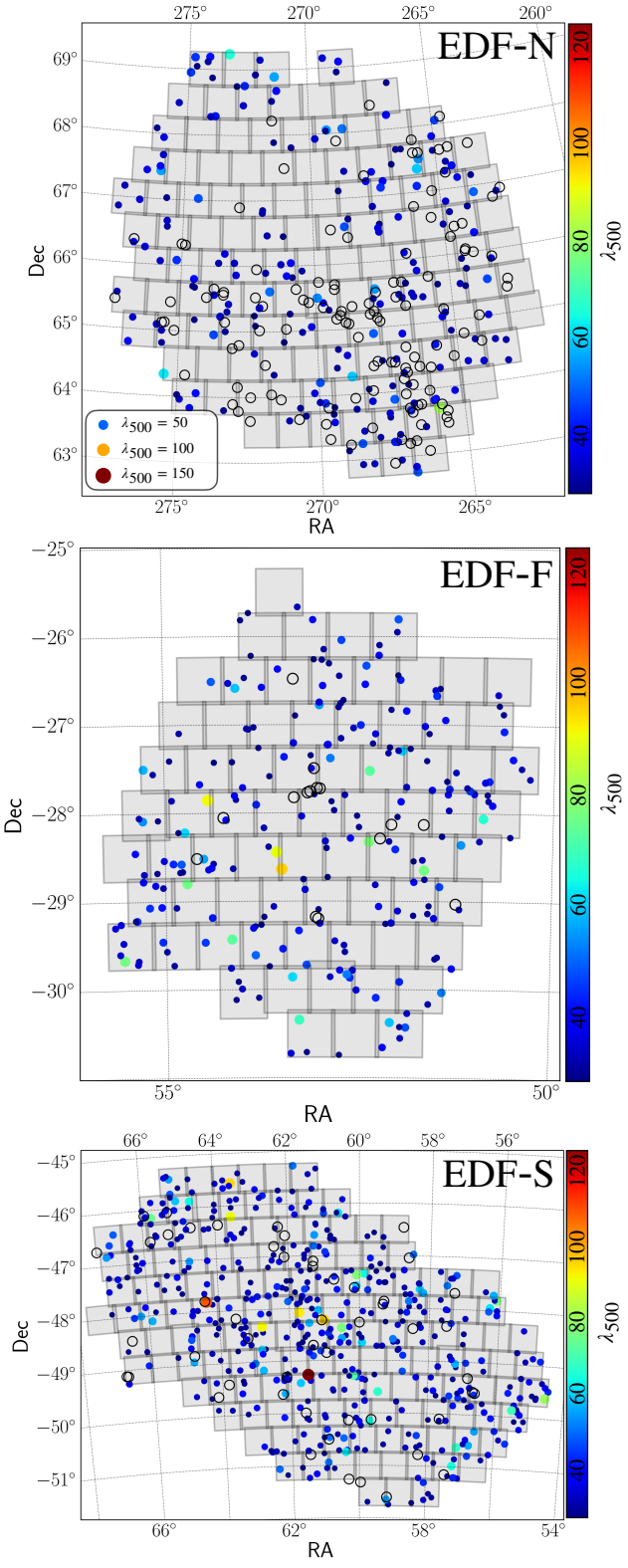

Fig. 1. Spatial distribution of galaxy clusters in the DLS and GCWG samples (see Sect. 3.1). From top to bottom: Three zoomed-in views of the Euclid Deep Field North (EDF-N), Euclid Deep Field Fornax (EDF-F), and Euclid Deep Field South (EDF-S) regions. Dot colours and sizes are scaled according to cluster richness, while empty circles mark clusters for which the richness values were not measured by Wen & Han (2024). A richness cut at $\lambda_{500} > 30$ was applied to the catalogue by Wen & Han (2024) to select the galaxy clusters for visual inspection.

mum (FWHM) of 0.″3 and AB magnitude of 24.5 within an aperture of diameter 1.″3. Observations in the near-IR bands achieves S/N $\geq$ 5 for point sources with an AB magnitude of 24.0 (Euclid Collaboration: Mellier et al. 2025; Euclid Collaboration: Cropper et al. 2025). The I_E, Y_E, J_E, and H_E images have a spatial sampling of 0.″1 per pixel, equivalent to the native pixel scale of the I_E images, and a point-spread function of approximately 0.″13, 0.″35, 0.″34, and 0.″35 FWHM, respectively (Euclid Collaboration: Mellier et al. 2025; Laureijs et al. 2011; Euclid Collaboration: Jahnke et al. 2025). Although the original spatial sampling of the Y_E, J_E, and H_E images is 0.″3 per pixel, it is oversampled to match the I_E pixel scale by the *Euclid* data-reduction pipeline.

This work aimed to visually identify strong-lensing features in *Euclid* data. To achieve this, we created colour images by combining *Euclid* observations in different bands. These images were obtained using the following method, which preserves the native higher resolution of the I_E filter. To begin, we employed the `STIFF` software (Bertin 2012) to create colour images in the red-green-blue (RGB) colour space. Specifically, we used the H_E, Y_E, and I_E bands for the red, green, and blue channels, respectively. We adopted the automatic sky background intensity and colour balance implemented in `STIFF`, and manually adjusted the contrast and brightness to provide satisfactory visibility of low-surface-brightness sources.

The spatial resolution of these images is penalised by the equal weighting of the I_E and near-IR bands. To improve the perceived spatial resolution, we performed a two-step image manipulation. First, we mapped the images from the RGB to the CIELAB colour space. The latter expresses colour as three values: L for perceptual lightness, and a and b for the four unique colours of human vision- red, green, blue, and yellow. We then substituted the L channel with the image in the I_E band. Finally, we mapped the image back to RGB colour space. The images were saved in the well-known Tagged Image File Format (TIFF).

This process results in images whose spatial resolution is driven by the I_E band, while the colour information is retained from the combination of H_E, Y_E, and I_E observations. As a result, the visibility of small-scale morphological features in the sources is greatly enhanced. For example, compact star-forming regions in distant galaxies are much better resolved in the I_E than in the near-IR bands and, therefore, are more clearly visible in the colour images created with the procedure outlined above than in the RGB image initially created with `STIFF`.

The methodology employed to prepare the colour images is often used in astrophotography for visualisation purposes only. These images are unsuitable for scientific analysis (e.g. performing multi-band photometry or measuring photometric redshifts). However, our aim was to visually identify strong-lensing features. This task was facilitated by the higher resolution and colour contrast achieved with the image processing that we have outlined. An additional caveat is that using the I_E band for the lightness channel dims the features only visible in the near-IR bands. For example, I_E-dropout sources appear strongly attenuated in our colour images. Due to this effect, we expect that a small fraction of strong-lensing features associated with background sources dropping out in the I_E band may have been missed during visual inspection. However, we emphasise that the use of RGB images preserving the I_E resolution, as adopted in our analysis, was often crucial for the secure identification of strong-lensing features. Furthermore, the lower resolution of the Near Infrared Spectrometer and Photometer (NISP) images, combined with light contamination from cluster member galaxies and intracluster light in near-IR bands, makes the detection of dropout lensed sources particularly challenging, even when using standard RGB images without a lightness channel. This limitation is expected to be mitigated in the near future, when convolutional neural networks will be employed to identify lensing clusters in the *Euclid* data (e.g. Euclid Collaboration: Bazzanini et al. 2026). In that case, the networks will be trained directly on single-band *Euclid* images, rather than on RGB composites.

3. Methodology

In this section, we describe the sample of visually inspected galaxy clusters (hereafter the VI catalogue), created by combining two main galaxy cluster catalogues (see Sect. 3.1). Section 3.2 presents the new visual inspection tool, specifically developed for this project. The visual inspection methodology is detailed in Sect. 3.3.

3.1. Galaxy cluster catalogue

To carry out the proposed experiment, we first considered the galaxy cluster catalogue presented by Wen & Han (2024), based on multi-band photometry from the DESI Legacy Imaging Surveys Data Release (DR) 9 and 10 (Dey et al. 2019) and the Wide-field Infrared Survey Explorer (WISE; Wright et al. 2010). In summary, they used four optical bands (g, r, i, and z) and two mid-infrared bands (W1 and W2). Photometric information was complemented with available spectroscopy from the Two Micron All-Sky Survey (2MASS; Huchra et al. 2012), the Sloan Digital Sky Survey DR17 (SDSS DR17; Abdurro'uf et al. 2022), and the Dark Energy Spectroscopic Instrument Early Data Release (DESI EDR; DESI Collaboration 2024). Galaxy clusters were identified as overdensities of stellar mass in galaxies centred on the brightest cluster galaxy (BCG) candidates within a redshift bin of $\Delta z = 0.04(1+z)$ for $z \leq 0.7$ or $\Delta z = 0.15\,z - 0.037$ for $z > 0.7$. Wen & Han (2024) identified BCGs based on their r, z, and W1 magnitudes, estimated redshifts, and stellar masses $M_* \geq 10^{11}\,M_\odot$. The publicly available catalogue lists about 1.58 million candidate galaxy clusters, of which 7446 are located within the Q1 footprint. We then applied a richness cut of $\lambda_{500} > 30$, resulting in 939 galaxy clusters (hereafter, DLS galaxy clusters). As shown in Fig. 2, this is equivalent to applying a cut of $M_{500} \gtrsim 1.36 \times 10^{14}\,M_\odot$. The spatial distribution of the DLS galaxy clusters in the three Q1 fields is shown in Fig. 1, colour-coded according to the estimated value of λ_{500} by Wen & Han (2024).

As discussed in Wen & Han (2024), although their photometric selection has good completeness (80% – 94%, depending on the survey considered for the comparison), some galaxy clusters remain unidentified. Thus, we complement the DLS galaxy cluster sample with a compilation created by merging 15 catalogues of known galaxy clusters (courtesy of Jean-Baptiste Melin; see also Euclid Collaboration: Bhargava et al. 2026). In detail, it includes galaxy clusters visible in the Q1 and DR1 footprints from the following catalogues (the number of Q1 systems is given in parentheses): the Meta-Catalogue of the compiled properties of X-ray detected Clusters of galaxies (MCXC; Piffaretti et al. 2011; Sadibekova et al. 2024, 35 galaxy clusters); the extended ROentgen Survey with an Imaging Telescope Array (eROSITA) cluster catalogue (Bulbul et al. 2024; Kluge et al. 2024, 125 galaxy clusters); the Meta Catalogue of SZ clusters (MCSZ; see Euclid Collaboration: Bhargava et al. 2026, 28 galaxy clusters); the Combined *Planck*-RASS catalogue of X-ray–SZ sources (ComPRASS; Tarrío et al. 2019, six galaxy

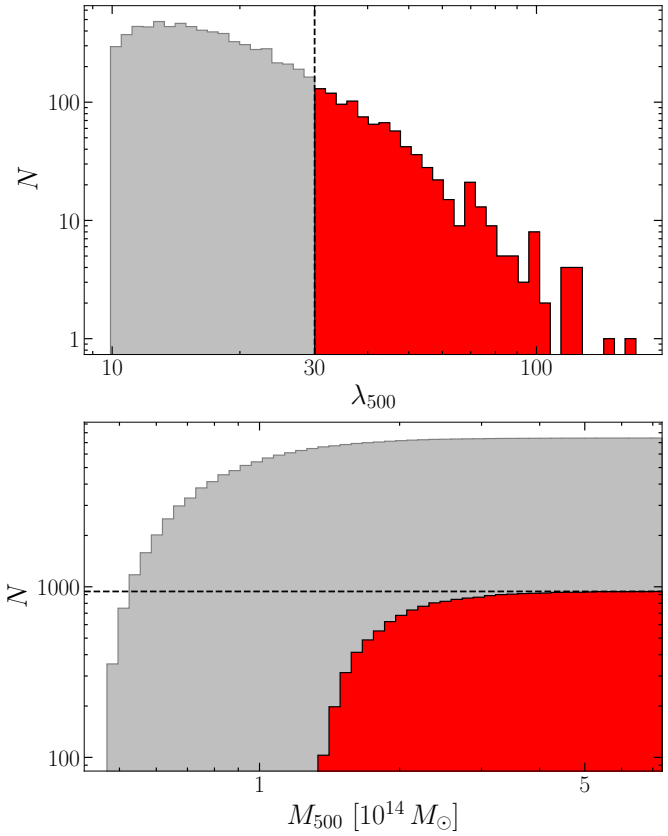

Fig. 2. Richness and mass distributions of galaxy clusters in Q1 from the catalogue of Wen & Han (2024). The top panel shows the distribution of cluster richness values (λ_{500}), while the bottom panel presents the cumulative distribution of cluster total masses (M_{500}). Grey histograms represent galaxy clusters in Q1 detected in the DESI Legacy Imaging Surveys by Wen & Han (2024), whereas red distributions correspond to the 939 clusters with $\lambda_{500} > 30$.

clusters); the Meta-Catalogue of Cluster Dispersions (MCCD; see Euclid Collaboration: Bhargava et al. 2026, two galaxy clusters); the RedMaPPer galaxy cluster catalogue from the Dark Energy Survey science verification data (RM DES; Rykoff et al. 2016; Abbott et al. 2020, 177 galaxy clusters); the catalogue of clusters of galaxies identified from the Sloan Digital Sky Survey by Wen et al. (2012, WHL SDSS; 142 galaxy clusters); the Abell catalogue of rich clusters (Abell 1958; Abell et al. 1989, 23 galaxy clusters); the MARD-Y3 catalogue (Klein et al. 2019, 19 galaxy clusters); the XMM CLuster Archive Super Survey catalogue (X-CLASS; Koulouridis et al. 2021, seven galaxy clusters); the PSZSPT catalogue (Melin et al. 2021, 10 galaxy clusters); the PSZ-MCMF catalogue of *Planck* clusters over the DES region (Hernández-Lang et al. 2023, seven galaxy clusters); the SPT-SZ MCMF cluster catalogue (Klein et al. 2024a, 13 galaxy clusters); the RASS-MCMF cluster catalogue (Klein et al. 2023, 44 galaxy clusters); and the ACT-DR5-MCMF galaxy cluster catalogue (Klein et al. 2024b, 21 clusters). From this sample, 484 unique galaxy clusters (i.e. those at least 1.′5 apart) fall within the Q1 footprint, of which 117 are not included in Wen & Han (2024). We refer to this sample as the GCWG (galaxy cluster working group) sample. The spatial distribution of these galaxy clusters in the three Q1 fields, marked as empty black circles, is shown in Fig. 1.

In summary, to build the sample of galaxy clusters to be considered for visual inspection (the VI catalogue), we combined the 939 DLS systems with the GCWG sample, resulting in a final catalogue of 1056 strong-lensing cluster candidates. Additionally, we removed ten galaxy clusters from the DLS catalogue with projected separations smaller than 1.′5.. These occurrences are not duplicate candidate galaxy clusters, but systems lying angularly close at different redshifts. Since the *Euclid* image cutouts adopted for visual inspection have a size of $4' \times 4'$ (see Sect. 2), both systems were visually inspected within a single cutout. Finally, we excluded 220 galaxy clusters located close to the boundaries of the Q1 tiles, whose cutouts contain more than 50% null values. The final number of cutouts for the visual inspection is therefore 826.

3.2. The `galaxyvote` platform

For the visual inspection of the *Euclid* images, we used the `galaxyvote` web application (Meneghetti et al., in prep.). A brief description of its functionalities is provided below.

The application back-end uses the `Flask` framework[1] to define routes (URLs) for the web application and associates them with `Python` functions. These functions interact with a relational database containing several tables. The software supports multiple experiments using different image collections, provides access to many users, and manages assignments. Additional tables enable the storage of grades, comments, and geometrical figures drawn by users to mark specific regions of the images. The application front-end is based on HTML and `JavaScript`. It employs the `Bootstrap CSS` framework[2] to design and style responsive and modern web pages efficiently.

For a given visual inspection experiment, a configuration script initialises the application database and populates it with the list of images and authorised users. These users log in with pre-assigned credentials to access their dedicated workspaces. Administrators set the number of users assigned to evaluate each image during the configuration. The system optimally creates the assignments based on the number of users and images. Each user's workspace contains a gallery of assigned images.

The users inspected the *Euclid* images through a web page containing the following features.

- An 800×800 pixel viewer enables image visualisation. We used the javascript library `OpenSeaDragon` for smooth image navigation, including mouse-enabled zoom-in and zoom-out functions. Users can opt to enter full-screen mode to improve their visualisation experience. To speed up image panning and scrolling, we tiled the images, converting them into the pyramidal Deep Zoom Image (DZI) format[3]. `OpenSeaDragon` supports several image-serving protocols for tiled sources, including DZI.
- Basic filters such as contrast and brightness adjustments enable users to improve the visibility of specific sources. These filters are implemented using the `OpenSeaDragonFiltering` add-on[4].
- A rectangle drawing tool. Users can draw rectangles within the image viewer to mark the positions of interesting features in the image and save them to the database. For our experiment, we asked users to draw rectangles on gravitational arcs and arclets, and sets of multiple images of background sources.

[1] https://flask.palletsprojects.com/en/stable/
[2] https://getbootstrap.com/
[3] https://shorturl.at/oZe52
[4] https://github.com/usnistgov/OpenSeadragonFiltering

– A voting panel. Users are asked to classify the inspected image. For our experiment, we set up three classes, namely: 'Certain Lens' (A), if the image contains any features that the user associates with a strong-lensing effect with extremely high confidence; 'Probable Lens' (B) if the detected features suggest a strong-lensing effect, but with lower confidence; and 'No Lens' (C) if the user does not detect any strong-lensing feature.
– A comment box. Users can provide feedback on their feature identifications. In particular, for our experiment, users were instructed to explain why they believed that strong-lensing effects could explain the detected features. In addition, they could describe their identifications in more detail if they wanted.

3.3. The visual inspection

While the primary aim of this experiment was to uncover new strong-lensing galaxy clusters, all inspectors were instructed to vote for any strong-lensing feature, regardless of whether it occurs in galaxy-, group-, or cluster-scale systems. The team of inspectors comprised 44 members of the Euclid Consortium, approximately half of whom are specialists in strong lensing by galaxy clusters and are thus very familiar with cluster-scale strong-lensing features.

The visual inspection experiment was divided into two stages, as described below. The inspectors had no access to information about the galaxy clusters' properties, such as coordinates, redshift, richness, or total mass, during the entire visual inspection process, thus ensuring a blind search for strong-lensing features.

The first stage consists of a 'calibration phase' in which the 44 inspectors voted on a subsample of galaxy clusters contained in the GCWG sample (a total of 434 cutouts, see Sect. 3.1). This collection of candidates was large enough to train the inspectors for the second phase. The number of assignments for each inspector varied between 55 and 87 so that each cutout could receive seven votes. This number of votes was determined to be the optimal compromise between the total required votes and the need for a robust final grade (e.g. Rojas et al. 2023; Schuldt et al. 2025). The primary aim of this phase was to train the inspectors to identify cluster-scale lenses and to familiarise them with the visual inspection tool. Additionally, this phase was used to identify possible software bugs and to implement feedback on potential improvements in the second, larger stage. Duplicate entries in the GCWG sample were not removed during this phase, enabling an evaluation of how the same object was ranked by different groups of inspectors or by the same inspector at different times. The calibration phase was completed by 40 of the 44 inspectors involved, collecting 88% of the expected number of votes in about a week.

The second stage examined the 826 *Euclid* images in the complete VI catalogue presented in Sect. 3.1. This phase involved 44 inspectors, 38 of whom completed the inspection in about three weeks. Thus, we collected 90% of the expected grades. As in the calibration phase, we aimed to collect seven grades per image. The number of assignments per inspector varied between 113 and 163.

Since not all inspectors were able to complete the voting procedures for the calibration phase and Phase 2 within the allocated time frame, some clusters received fewer than the requested seven votes by the end of the visual inspection process. Specifically, in Phase 2, only ten cluster images out of 826 received fewer than five votes (with one cluster receiving three votes and nine receiving four), while 89% of the images received six or more votes. This number of votes, closely approaching the target of seven, ensures the robustness of our results. Additionally, four inspectors who participated in Phase 2 did not participate in the training (calibration) phase. For these inspectors, we verified that the distribution of A, B, and C grades they assigned closely resembled the vote distribution of inspectors who participated in both phases. Two of the four inspectors are recognised experts in the field, for whom the calibration phase would have primarily served as an opportunity to familiarise themselves with the software, rather than to learn how to identify cluster lenses.

4. Results

In each phase, a score value of being a strong gravitational lens, $\mathcal{P}_{\rm lens}$, was assigned to each cluster. This score was computed as

$$\mathcal{P}_{\rm lens} = \frac{N_{\rm A} + 0.5\,N_{\rm B}}{N_{\rm A} + N_{\rm B} + N_{\rm C}}\,, \tag{1}$$

where $N_{\rm A}$, $N_{\rm B}$, and $N_{\rm C}$ were the numbers of A, B, and C grades given to the image, respectively.

A value of $\mathcal{P}_{\rm lens} = 1$ was assigned only if all inspectors evaluated the cluster as a secure gravitational lens (all A grades). Conversely, a value of $\mathcal{P}_{\rm lens} = 0.5$ indicates that all inspectors were uncertain about the presence of strong-lensing features (all B grades) and/or that the number of A grades (secure presence) is equal to the number of C grades (secure absence). In the following two sections, which present the main results from the two phases of visual inspection, we consider clusters with $\mathcal{P}_{\rm lens} > 0.5$ as potential strong gravitational lenses. This threshold ensures that at least one inspector classified the candidate lensing cluster as a secure lens (grade A), and that the number of A grades exceeds the number of C grades. To further assess the reliability of our findings, particularly given that some clusters received fewer than the intended seven votes, we estimated the uncertainty associated with the lensing scores, $\mathcal{P}_{\rm lens}$. For each cluster, we performed 1000 realisations of $\mathcal{P}_{\rm lens}$, obtained by random sampling from the distribution of A, B, and C grades it received. The uncertainty was then computed from the 16th and 84th percentiles of the resulting $\mathcal{P}_{\rm lens}$ distribution.

4.1. Calibration phase

The calibration phase returned 25 strong-lensing clusters with $\mathcal{P}_{\rm lens} > 0.5$, listed in Table 1. In Fig. 3, we show the three cluster lenses with $\mathcal{P}_{\rm lens} = 1$. As evident from the table, there is a wide range in the total number of votes, $N = N_{\rm A} + N_{\rm B} + N_{\rm C}$, assigned to some clusters. For instance, the two clusters ACT-CLJ0411.2−4819 and RMJ040125.7−475359.1 have N equal to 49 and 4, respectively. These differences arise from the presence of 60 duplicate clusters that appeared at least twice in the GCWG sample; consequently, their images received more grades than clusters without duplicates. To test the robustness and self-consistency of the visual inspection methodology, we plot the differences between the $\mathcal{P}_{\rm lens}$ values assigned to different occurrences of the same clusters as a grey histogram in Fig. 4. For more than 50% (90%) of the duplicates, the difference in $\mathcal{P}_{\rm lens}$ is less than 0.09 (0.26). This analysis shows that the strong-lensing score is only marginally affected by variations in the group of inspectors or by the same inspector voting at different times. As an additional test, Fig. 5 shows the fraction of A, B, and C votes assigned by each inspector to the visually inspected clusters. Inspectors without prior experience in strong gravitational lensing by galaxy clusters are marked with red IDs on the horizontal axis. Specifically, the average and standard deviation

Table 1. Galaxy clusters in the calibration phase (GCWG sample) with $\mathcal{P}_{\rm lens} > 0.5$, indicative of being strong gravitational lenses.

Name	RA (J2000)	Dec (J2000)	$N_{\rm A}$	$N_{\rm B}$	$N_{\rm C}$	$\mathcal{P}_{\rm lens}$
RMJ040125.7−475359.1	60.35721	−47.89974	4	0	0	$1.00^{+0.00}_{-0.00}$
RMJ035713.8−475646.8	59.30752	−47.94633	14	0	0	$1.00^{+0.00}_{-0.00}$
RMJ035250.8−492809.2	58.21182	−49.46921	6	0	0	$1.00^{+0.00}_{-0.00}$
ACT-CLJ0411.2−4819	62.80204	−48.31183	53	1	0	$0.99^{+0.01}_{-0.01}$
J180522.2+635735	271.34250	63.95965	6	0	1	$0.86^{+0.14}_{-0.15}$
RMJ033906.2−283952.0	54.77564	−28.66445	5	0	1	$0.83^{+0.17}_{-0.16}$
ACT-CLJ0417.3−4748	64.36486	−47.80644	31	15	1	$0.82^{+0.04}_{-0.04}$
ACT-CLJ0414.2−4612	63.55490	−46.20033	24	9	2	$0.81^{+0.06}_{-0.04}$
J175226.0+640222	268.10834	64.03943	4	3	0	$0.79^{+0.07}_{-0.08}$
ACT-CLJ0406.8−4804★	61.72112	−48.08194	17	11	1	$0.78^{+0.05}_{-0.06}$
RMJ040205.1−480808.6	60.52128	−48.13571	4	2	1	$0.71^{+0.15}_{-0.14}$
RMJ040512.7−470602.2	61.30275	−47.10061	4	2	1	$0.71^{+0.15}_{-0.14}$
RMJ040202.3−483429.6	60.50947	−48.57489	2	3	0	$0.70^{+0.10}_{-0.10}$
ACT-CLJ0348.7−4902	57.19855	−49.03517	6	7	1	$0.68^{+0.07}_{-0.07}$
ACO2281	265.75434	64.64593	3	2	1	$0.67^{+0.16}_{-0.17}$
MARDJ032632.1−283916	51.63379	−28.65462	2	5	0	$0.64^{+0.07}_{-0.07}$
ACT-CLJ0357.8−4859	59.47237	−48.99443	11	11	4	$0.63^{+0.08}_{-0.07}$
RMJ033859.1−281343.8	54.74643	−28.22884	4	7	1	$0.63^{+0.09}_{-0.08}$
RXJ1745.2+6556	266.31750	65.93810	2	1	1	$0.63^{+0.26}_{-0.24}$
1eRASSJ040349.4−501834	60.95596	−50.30948	4	8	1	$0.62^{+0.07}_{-0.08}$
MARDJ035850.4−500844	59.71026	−50.14557	11	16	5	$0.59^{+0.07}_{-0.06}$
J174145.3+650415	265.43884	65.07072	4	6	2	$0.58^{+0.13}_{-0.08}$
1eRASSJ033203.2−264635	53.01357	−26.77665	1	5	0	$0.58^{+0.09}_{-0.08}$
RMJ040520.8−485427.1	61.33676	−48.90753	2	4	1	$0.57^{+0.14}_{-0.14}$
ACT-CLJ0405.9−4915★†	61.49234	−49.26265	16	33	11	$0.54^{+0.04}_{-0.04}$

Notes. For each galaxy cluster, we report the total number of A, B, and C grades ($N_{\rm A}$, $N_{\rm B}$, and $N_{\rm C}$) assigned by the inspectors. The uncertainty in the lensing score is computed as described in Sect. 4. The star (★) and dagger (†) symbols mark gravitational lenses previously observed with the *Hubble* Space Telescope and *James Webb* Space Telescope, respectively.

of the total number of A, B, and C votes assigned by the group of lensing experts in the calibration phase are: $N^{\rm tot}_{\rm A,ex} = 7 \pm 4$, $N^{\rm tot}_{\rm B,ex} = 22 \pm 10$, and $N^{\rm tot}_{\rm C,ex} = 38 \pm 14$. Similarly, for the group of non-experts, the values are: $N^{\rm tot}_{\rm A,non\text{-}ex} = 7 \pm 3$, $N^{\rm tot}_{\rm B,non\text{-}ex} = 18 \pm 8$, and $N^{\rm tot}_{\rm C,non\text{-}ex} = 43 \pm 12$. These values reveal no significant correlation between the number of votes and user expertise, as the observed fluctuations are consistent with variance in lensing cluster numbers across the inspected samples. The calibration phase did not reveal any major bugs in the visual inspection tool described in Sect. 3.2, which was therefore adopted for the second phase.

4.2. Phase 2

In Table A.1, we list the 76 strong gravitational lensing clusters with $\mathcal{P}_{\rm lens} > 0.5$, identified during the second visual inspection phase from the VI catalogue. In this phase, the inspectors identified 13 secure cluster lenses ($\mathcal{P}_{\rm lens}$=1), four of which were already found during the calibration phase. The galaxy clusters RMJ040125.7−475359.1 and RMJ035713.8−475646.8 were classified as secure lenses in both phases, while ACT-CLJ0411.2−4819 and ACT-CLJ0414.2−4612 had previously been assigned scores of $\mathcal{P}_{\rm lens} = 0.99^{+0.01}_{-0.01}$ and $\mathcal{P}_{\rm lens} = 0.81^{+0.06}_{-0.04}$, respectively, in the calibration phase. Conversely, the galaxy cluster RMJ035250.8−492809.2, identified as a secure lens in the first phase, is absent from the VI catalogue due to the richness cut of $\lambda_{500} > 30$ applied during its creation. Specifically, Wen & Han (2024) estimate a richness value of $\lambda_{500} = 28.61$ for this cluster. In Figs. 6, 7, and 8, we show the additional 11 secure cluster lenses identified in the second phase. When comparing Table A.1 and Table 1, we find that six galaxy clusters, similarly to

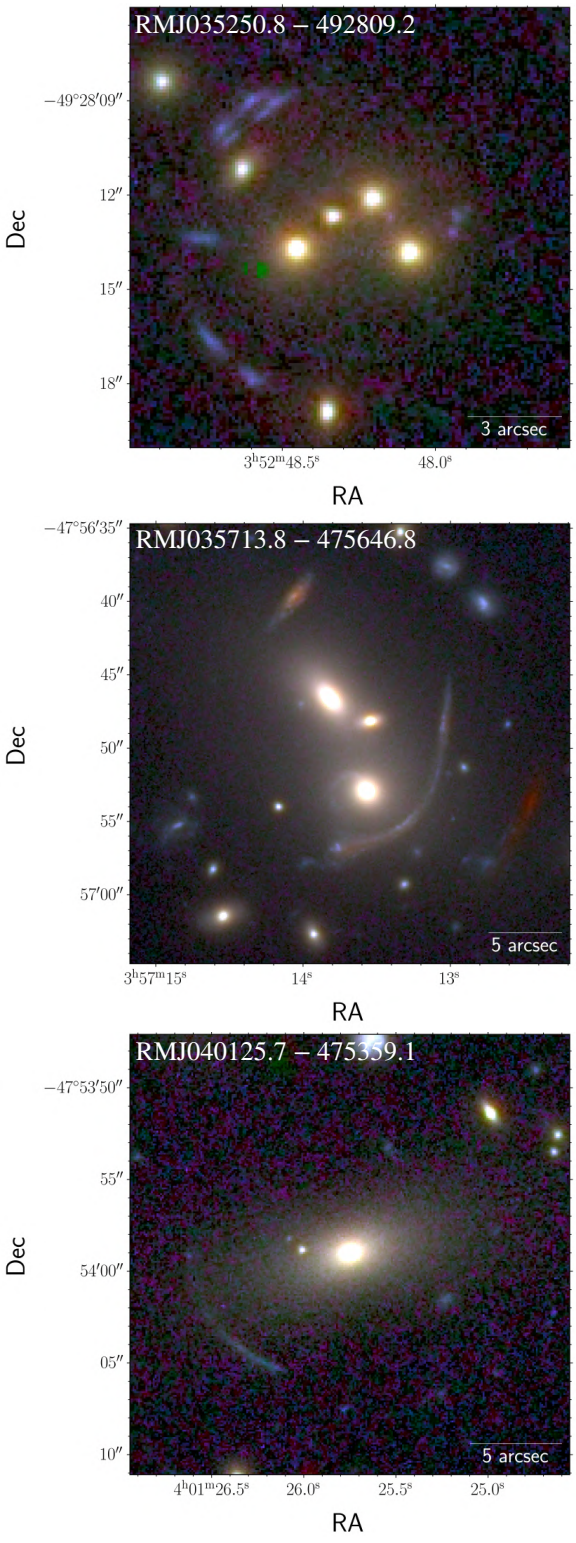

Fig. 3. Three secure galaxy cluster strong gravitational lenses ($\mathcal{P}_{\rm lens}$ = 1) identified in the calibration phase (GCWG sample). Two of the clusters, RMJ035713.8−475646.8 and RMJ040125.7−475359.1, are also identified as secure lenses in the Phase 2 run (see Sect. 4.2).

RMJ035250.8−492809.2, appear exclusively in the latter table. Specifically, J180522.2+635735 and ACT-CLJ0357.8−4859 have $\lambda_{500} < 30$ and are therefore not included in the VI catalogue. The remaining four clusters, RMJ040512.7−470602.2, MARDJ032632.1−283916, 1eRASSJ033203.2−264635, and

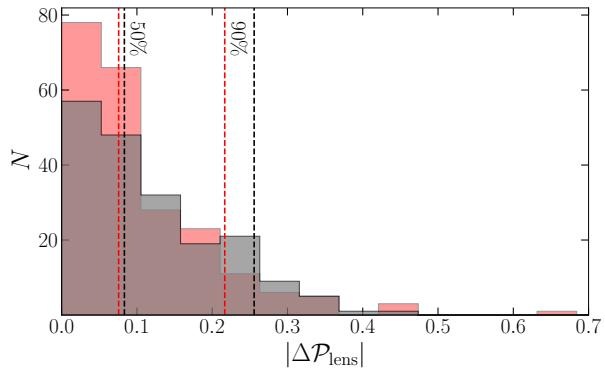

Fig. 4. Difference between the $\mathcal{P}_{\rm lens}$ values, $\Delta\mathcal{P}_{\rm lens}$, assigned to the same clusters by different groups of inspectors and/or at different times. The black distribution corresponds to the $\Delta\mathcal{P}_{\rm lens}$ obtained for different occurrences of the same cluster in the GCWG sample during the calibration phase of the visual inspection. The red distribution shows the comparison between the $\mathcal{P}_{\rm lens}$ values assigned to the same clusters in the calibration phase and in Phase 2. Vertical dashed black and red lines mark the 50th and 90th percentiles of the corresponding $\mathcal{P}_{\rm lens}$distributions, respectively.

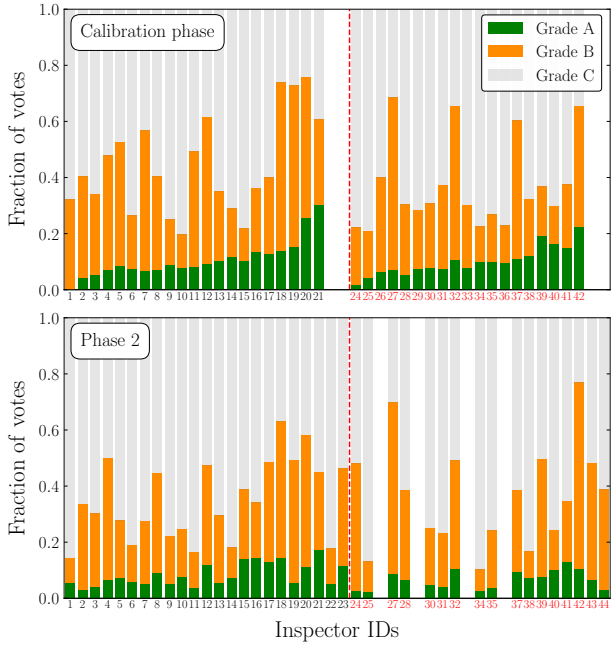

Fig. 5. Fractions of A, B, and C grades assigned by each inspector, identified by unique numerical IDs, to candidate cluster lenses. The results from the calibration phase and from Phase 2 are shown in the upper and lower panels, respectively. Inspectors with little or no experience in strong gravitational lensing by galaxy clusters are marked with red IDs. A vertical dashed red line separates lensing experts from non-experts. Inspectors who graded fewer than two clusters are not included.

RMJ040520.8−485427.1, received lensing scores of $0.5^{+0.14}_{-0.14}$, $0.5^{+0.07}_{-0.07}$, $0.5^{+0.0}_{-0.0}$, and $0.5^{+0.14}_{-0.07}$, respectively, during Phase 2. As these scores fall just below the threshold adopted for the selection of candidate cluster lenses, they are not listed in Table A.1. Notably, three of the four clusters exceed the threshold well within the 1σ uncertainty. The remaining system, 1eRASSJ033203.2−264635, which received only B votes in Phase 2, is characterised by a zero-width uncertainty distribution.

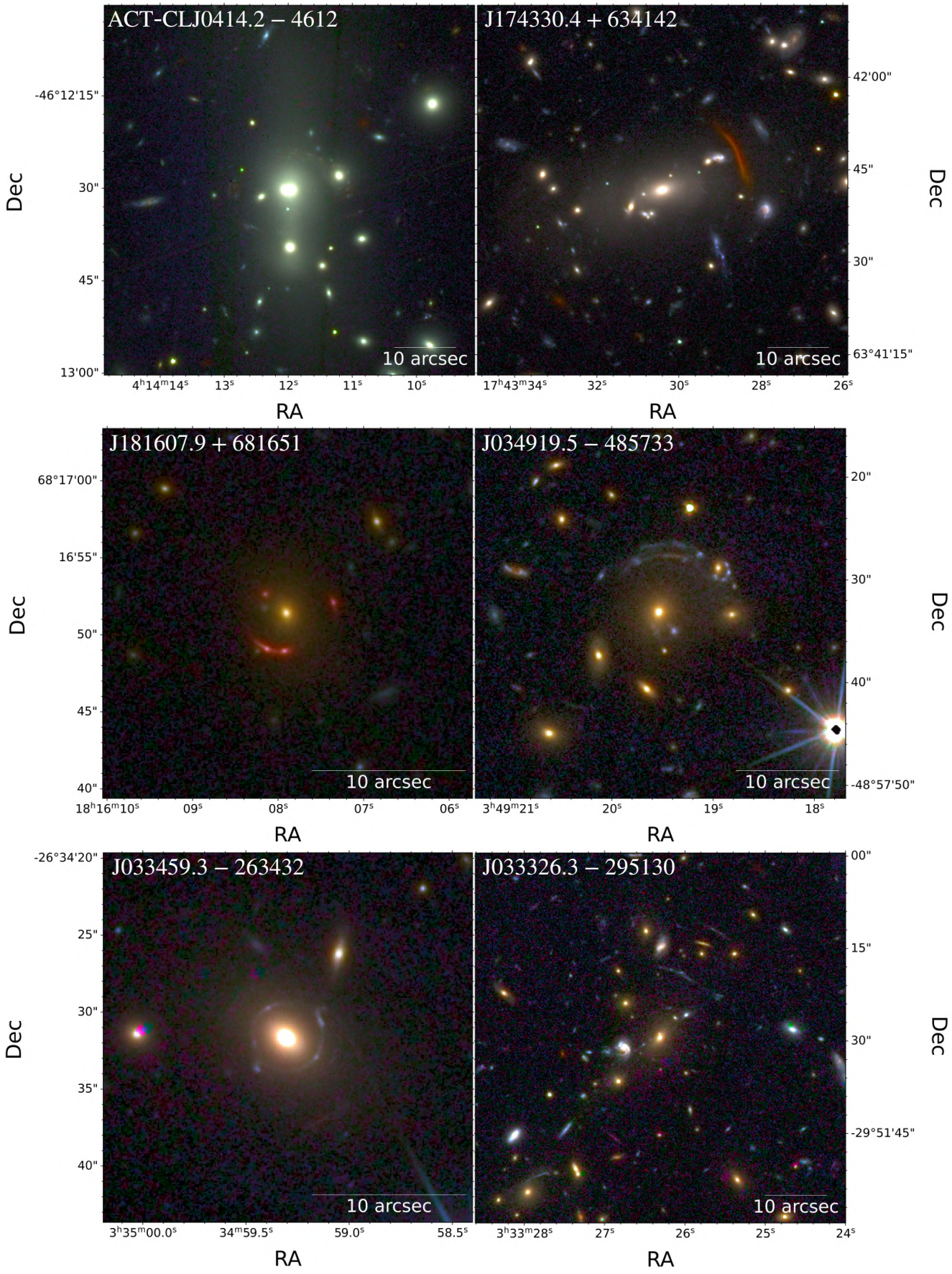

Fig. 6. Six of the 13 secure galaxy-cluster strong gravitational lenses ($\mathcal{P}_{\rm lens} = 1$) identified in the Phase 2 run (VI catalogue). The remaining seven secure Phase 2 lenses are shown in Figs. 7, 8, and 3.

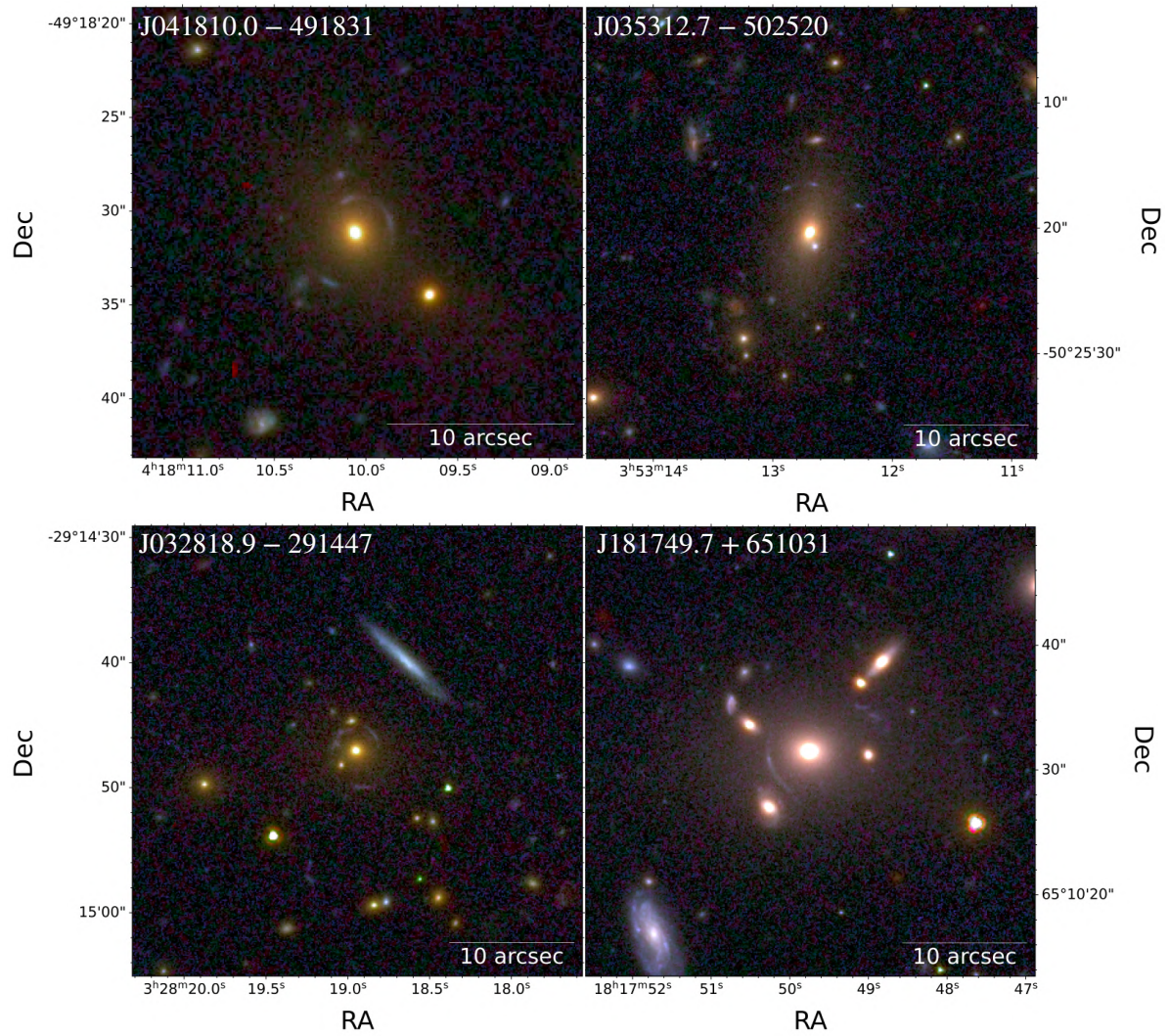

Fig. 7. Four of the 13 secure galaxy-cluster strong gravitational lenses ($\mathcal{P}_{\rm lens} = 1$) identified in the Phase 2 run (VI catalogue). The remaining nine secure Phase 2 lenses are shown in Figs. 6, 8, and 3.

Since 211 galaxy clusters visually inspected in the calibration phase were also re-inspected in Phase 2, we show the absolute differences between the $\mathcal{P}_{\rm lens}$ values assigned to the same clusters in the two phases as a red histogram in Fig. 4. This additional test demonstrates that most clusters were consistently ranked between the two visual inspection phases. Specifically, 90% of the analysed objects exhibit $\mathcal{P}_{\rm lens}$ differences of less than 0.22. As in the calibration phase, Fig. 5 presents the percentage of A, B, and C votes assigned to the clusters visually inspected by each user. Similarly, Phase 2 does not reveal any significant bias in vote distribution across inspectors or as a function of user expertise.

4.3. Characterisation of the physical properties of the lens clusters

Although a detailed study of the physical properties of the newly observed galaxy cluster strong gravitational lenses lies beyond the scope of this work, we present some preliminary results from our analysis in this section. In Fig. 9, we plot the distribution of cluster masses, M_{500}, as a function of redshift. Markers representing the visually inspected clusters are colour-coded according to their $\mathcal{P}_{\rm lens}$ values. The figure reveals that most galaxy cluster lenses lie in the redshift range $0.32 < z < 0.68$. This result is attributable to a combination of two main factors. First, the wavelength coverage of the *Euclid* photometric filters, the EWS image depth, and the higher resolution of the $I_{\rm E}$ band compared to the near-IR bands are designed to facilitate identification of most galaxies at $z < 2$. Secondly, as shown by Meneghetti et al. (2013, see also Meneghetti et al. 2023) using cosmological simulations, the lensing cross-section for giant arcs from sources at that redshift is maximised for cluster lenses at $z \simeq 0.3$.

Based on our census of galaxy cluster strong gravitational lenses identified in the 63.1 deg^2 covered by EDF-N, EDF-S, and EDF-F, we provide an estimate of the expected number density of cluster lenses per square degree detectable in the EWS. In Fig. 10, we show the number density of strong-lensing clusters, identified in Phase 2, as a function of the threshold lensing score. Specifically, we expect approximately 0.3 deg^{-2} cluster lenses with $\mathcal{P}_{\rm lens} > 0.9$. By lowering the lensing score threshold to $\mathcal{P}_{\rm lens} > 0.5$, the expected number density of strong-lensing clusters increases to 1.2 deg^{-2}. Given the final EWS sky coverage of approximately 14 000 deg^2, we predict that *Euclid* will detect more than 4200 cluster lenses exhibiting unequivocal evidence of extended, bright giant arcs and

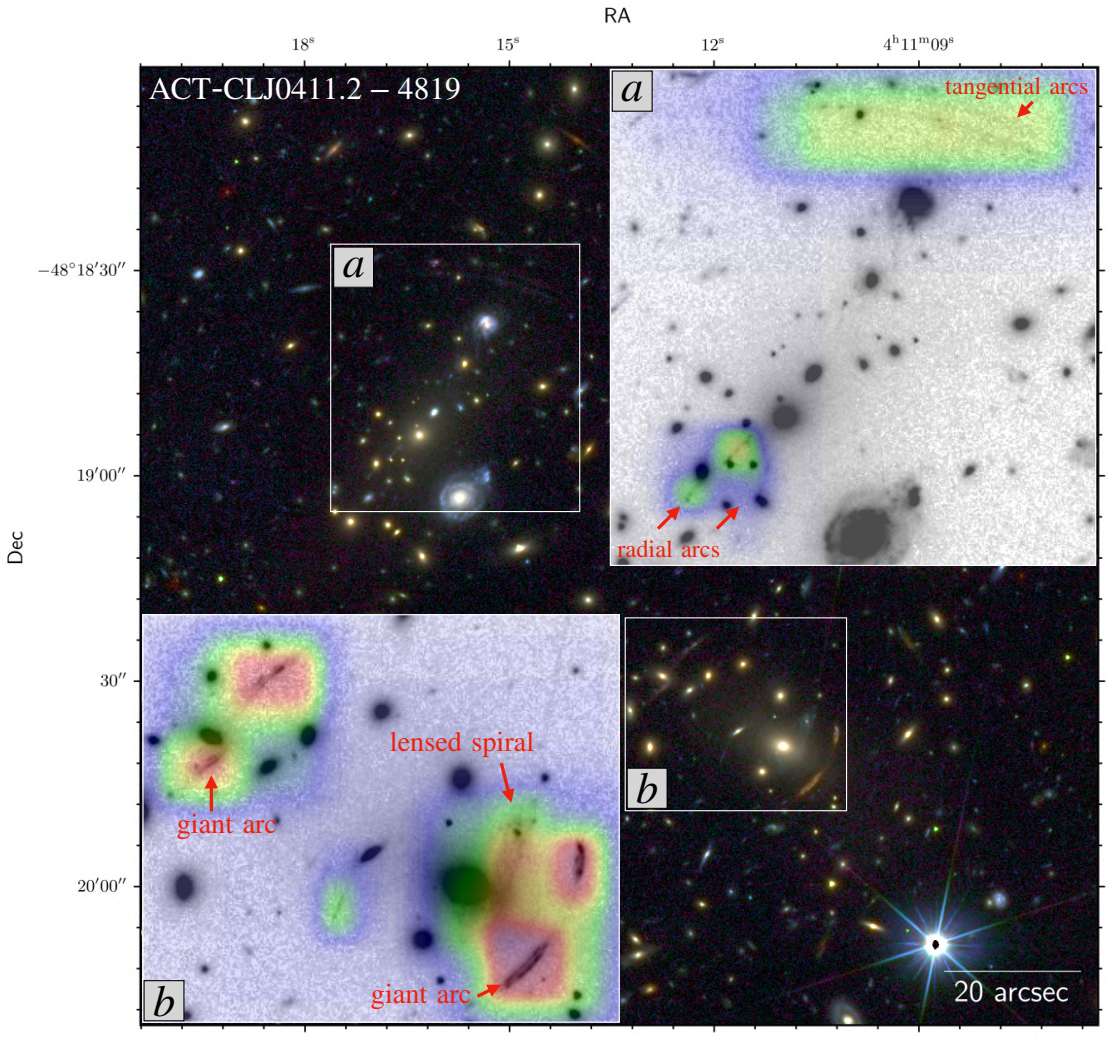

Fig. 8. Merging galaxy cluster identified as a secure gravitational lens in the second phase of the visual inspection. The zoom-ins centred on the two merging massive structures are superimposed, showing heat maps derived from rectangular regions drawn by the inspectors during the visual inspection process. These maps highlight various strong-lensing features, including tangential and radial arcs, as well as multiple images, with redder colours indicating more evident features.

multiple images. These estimates are likely conservative. The presented visual inspection relies entirely on cluster catalogues. Therefore, the estimated lensing cluster number density does not account for newly discovered cluster lenses not yet included in any existing catalogues. Additionally, the selection based on richness values and the large uncertainty affecting the λ_{500} values measured by Wen & Han (2024) could further impact our results.

In Fig. 8, we show as an example the rectangles drawn by the inspectors in the field of ACT-CLJ0411.2−4819, highlighting the strong-lensing features they identified. The red pixels, corresponding to regions where many rectangles overlap, indicate areas of the clusters containing prominent giant arcs and multiple images. These rectangles will provide the sample for training deep-learning models to automatically find similar features in future *Euclid* data.

Among the secure cluster lenses detected in Q1, the cluster identified as ACT-CLJ0411.2−4819, shown in Fig. 8, deserves special mention. This is a merging cluster that exhibits a variety of bright and extended strong-lensing features, including tangential and radial giant arcs at different redshifts. Additionally, several smaller galaxy groups surrounding the main cluster, each displaying evident strong-lensing features, make this cluster an excellent candidate for future follow-up observations.

Finally, we also identified several galaxy-galaxy strong lensing-events in cluster fields. This is expected since dense galaxy cluster environments enhance the strong-lensing cross-section of galaxies in these fields (e.g. Meneghetti et al. 2020).

5. Conclusions

We present the first catalogue of strong-lensing galaxy clusters observed by *Euclid*. These clusters are part of the catalogue of optically selected galaxy clusters by Wen & Han (2024), supplemented with other clusters. Most were observed from space for the first time, thanks to *Euclid*. For this reason, only a few of these galaxy clusters were previously known to host strong-lensing features. Thanks to the spatial resolution and depth of *Euclid* observations, we identified several gravitational arcs and multiple images of galaxies in the cluster backgrounds.

To detect these features and classify clusters as lenses or non-lenses, we visually inspected colour images created by combining *Euclid* observations in the I_E, Y_E, and H_E bands. The search was carried out blindly by 44 inspectors using a new

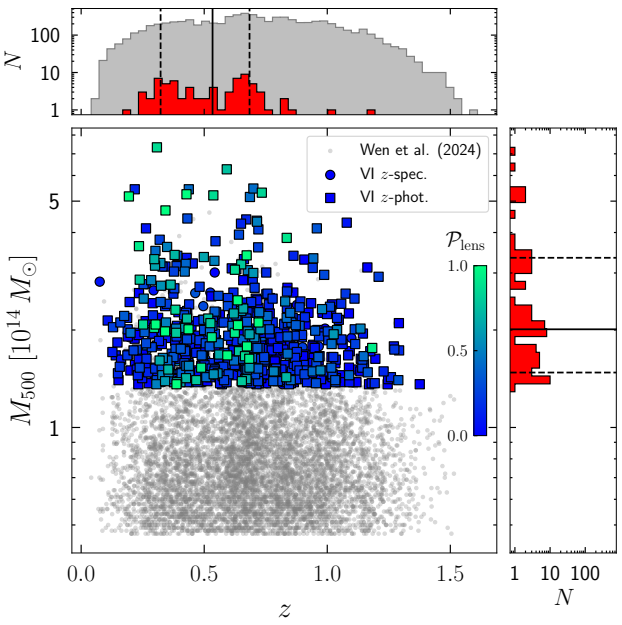

Fig. 9. Total mass-redshift distribution of the clusters visually inspected during the Phase 2 run. Small grey dots and histograms refer to galaxy clusters detected in the DESI Legacy Imaging Surveys by Wen & Han (2024) and located within the Q1 63.1 deg^2 area. Squares and dots correspond, respectively, to the galaxy clusters with measured photometric or spectroscopic redshifts, colour-coded by the lensing score, $\mathcal{P}_{\rm lens}$. The total mass and redshift distributions of clusters with $\mathcal{P}_{\rm lens} > 0.5$ are shown as red histograms, while black lines represent the 16th (dashed line), 50th (solid line), and 84th (dashed line) percentiles of these distributions. The effect of the selection criterion ($\lambda_{500} > 30$) adopted to select the clusters for visual inspection is evident.

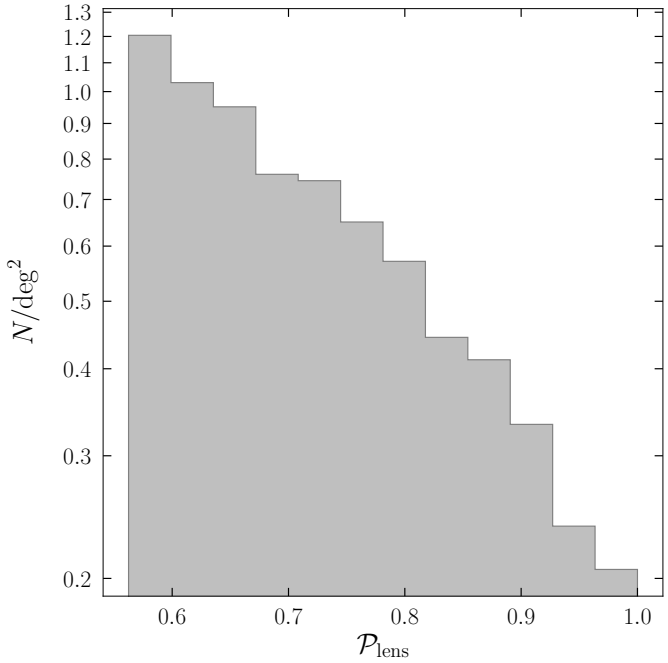

Fig. 10. Number density of galaxy clusters as a function of the threshold lensing score, $\mathcal{P}_{\rm lens}$, as assigned during the second phase of the visual inspection.

interactive visualisation tool. We identified 83 strong gravitational lenses among approximately one thousand galaxy clusters inspected during the calibration phase and Phase 2, 14 of which exhibit secure strong-lensing features such as tangential and radial arcs and multiple images. To our knowledge, only two arcs among those found had previously been identified in ground-based observations (the brightest arcs in J174330.4+634142, a.k.a. A2280, and ACT-CLJ0411.2−4819 Gioia et al. 1995; Bayliss et al. 2016). Only three of the identified gravitational lenses, marked with stars (⋆) in Tables 1 and A.1, were previously observed by the *Hubble* Space Telescope, with one of them, marked with a dagger (†), also observed by the *James Webb* Space Telescope. For the remaining 80 lenses, *Euclid* provides the first space-based optical observations and the spatial resolution necessary to discover many more strong-lensing features. Considering the number of newly observed lensing galaxy clusters and the high quality of *Euclid* imaging data, even at the depth of the EWS, *Euclid* will increase the sample of known gravitational lenses by more than an order of magnitude, paving the way for unprecedented advancement in the field of gravitational lensing by galaxy clusters.

In the sample we inspected, we find that approximately 0.3 clusters per square degree contain evident strong-lensing features. Based on this number density, we expect that *Euclid* will observe more than 4200 strong-lensing clusters in the EWS, assuming optical selection above a minimum richness of 30. This estimate is consistent with forecasts by Boldrin et al. (2016), based on simulations in the ΛCDM cosmological model, although the impact of the selection function requires further study.

The redshift distribution of the strong-lensing clusters in our sample peaks at $z \simeq 0.5$, consistent with expectations (e.g. Boldrin et al. 2012; Meneghetti et al. 2013; Boldrin et al. 2016). Based on the galaxy distributions, the sample does not appear to be biased in terms of cluster dynamical state. Few lenses show elongated or multimodal spatial distributions of galaxies that are likely cluster members. Other lenses have more axially symmetric distributions of cluster galaxies.

In the near future, we expect to find more strong-lensing clusters in the upcoming *Euclid* data. These observations will enable numerous new studies based on strong gravitational lensing, aimed at understanding the nature of dark matter and dark energy, constraining cosmological parameters, studying high-redshift sources, and more. For many of these lensing applications, combining *Euclid* data with complementary observations, including spectroscopy and observations in the X-ray, submillimetre, and radio domains, will be crucial. Exploiting the synergy between *Euclid* and optical time-domain surveys, in particular the Vera C. Rubin Observatory Legacy Survey of Space and Time (Guy et al. 2022), will also make possible the discovery of explosive transients that are gravitationally lensed by strong-lensing galaxy clusters.

Euclid is accumulating data at approximately 6.25 deg^2 per day. The rapid data volume growth renders our visual inspection approach inefficient for finding strong lenses. Given that the Phase 2 run took approximately three weeks to complete, we estimate that visually inspecting the entire EWS area, 222 times larger than the Q1 area, would require more than 13 years. As seen in searches for galaxy-galaxy strong lenses, citizen science may help mitigate this problem (Euclid Collaboration: Walmsley et al. 2026; Euclid Collaboration: Holloway et al. 2026). However, despite being less numerous, galaxy clusters are much more complex lenses than galaxies. They produce a variety of image configurations that inspectors cannot easily recognise without proper

training. For this reason, automating the search for strong-lensing features in galaxy clusters is a priority. In this work, we have identified several tens of gravitational arcs and arclets. We will combine these with simulated data to train deep-learning algorithms, such as different architectures of convolutional neural networks, to find features such as gravitational arcs, arclets, and multiple images.

Our work demonstrates the huge potential of the *Euclid* mission to discover new strong-lensing clusters. We have identified several lenses with multiple gravitational arcs, implying large strong-lensing cross-sections. These galaxy clusters will be re-observed by *Euclid* multiple times during the mission as part of the EDF survey. These observations will make it possible to identify additional arcs and multiple images by reaching fainter magnitude limits. Thus, we will collect many more observables to build robust total-mass models of these lenses. In addition, by comparing observations taken at different times, we may be able to detect lensed transients. The observations of such sources would facilitate further science cases. For example, in the case of multiply imaged time-variable sources, it may be possible to measure the cosmic expansion rate (Kelly et al. 2015, 2016; Grillo et al. 2015, 2018, 2024).

Acknowledgements. We acknowledge financial support through grants PRIN-MIUR 2017WSCC32 and 2020SKSTHZ. MM and PB acknowledge support from the Italian Space Agency (ASI) through contract "Euclid – Phase E", INAF Grants "The Big-Data era of cluster lensing" and "Probing Dark Matter and Galaxy Formation in Galaxy Clusters through Strong Gravitational Lensing". The research activities described in this paper have been co-funded by the European Union – NextGeneration EU within PRIN 2022 project no. 20229YBSAN – Globular clusters in cosmological simulations and in lensed fields: from their birth to the present epoch. AA acknowledges financial support through the project PID2022-138896NB-C51 (MCIU/AEI/MINECO/FEDER, UE) Ministerio de Ciencia, Investigación y Universidades. MJ is supported by the United Kingdom Research and Innovation (UKRI) Future Leaders Fellowship "Using Cosmic Beasts to uncover the Nature of Dark Matter" (grant number MR/S017216/1 and MR/X006069/1). This work has made use of the Early Release Observations (ERO) data from the *Euclid*/ mission of the European Space Agency (ESA), 2024, https://doi.org/10.57780/esa-qmocze3. This work has made use of the *Euclid* Quick Release Q1 data from the *Euclid*/ mission of the European Space Agency (ESA), 2025, https://doi.org/10.57780/esa-2853f3b. The Euclid Consortium acknowledges the European Space Agency and a number of agencies and institutes that have supported the development of *Euclid*, in particular the Agenzia Spaziale Italiana, the Austrian Forschungsförderungsgesellschaft funded through BMIMI, the Belgian Science Policy, the Canadian Euclid Consortium, the Deutsches Zentrum für Luft- und Raumfahrt, the DTU Space and the Niels Bohr Institute in Denmark, the French Centre National d'Etudes Spatiales, the Fundação para a Ciência e a Tecnologia, the Hungarian Academy of Sciences, the Ministerio de Ciencia, Innovación y Universidades, the National Aeronautics and Space Administration, the National Astronomical Observatory of Japan, the Netherlandse Onderzoekschool Voor Astronomie, the Norwegian Space Agency, the Research Council of Finland, the Romanian Space Agency, the State Secretariat for Education, Research, and Innovation (SERI) at the Swiss Space Office (SSO), and the United Kingdom Space Agency. A complete and detailed list is available on the *Euclid* web site (www.euclid-ec.org/consortium/community/). This work has made use of CosmoHub, developed by PIC (maintained by IFAE and CIEMAT) in collaboration with ICE-CSIC. CosmoHub received funding from the Spanish government (MCIN/AEI/10.13039/501100011033), the EU NextGeneration/PRTR (PRTR-C17.I1), and the Generalitat de Catalunya. Based on data from UNIONS, a scientific collaboration using three Hawaii-based telescopes: CFHT, Pan-STARRS, and Subaru www.skysurvey.cc. Based on data from the Dark Energy Camera (DECam) on the Blanco 4-m Telescope at CTIO in Chile https://www.darkenergysurvey.org. This work uses results from the ESA mission *Gaia*, whose data are being processed by the Gaia Data Processing and Analysis Consortium https://www.cosmos.esa.int/gaia.

References

Abbott, T. M. C., Aguena, M., Alarcon, A., et al. 2020, Phys. Rev. D, 102, 023509
Abdurro'uf, Accetta, K., Aerts, C., et al. 2022, ApJS, 259, 35
Abell, G. O. 1958, ApJS, 3, 211
Abell, G. O., Corwin, H. G., Jr, & Olowin, R. P. 1989, ApJS, 70, 1
Acebron, A., Grillo, C., Suyu, S. H., et al. 2024, ApJ, 976, 110
Atek, H., Gavazzi, R., Weaver, J., et al. 2025, A&A, 697, A15
Bayliss, M. B., Ruel, J., Stubbs, C. W., et al. 2016, ApJS, 227, 3
Bergamini, P., Grillo, C., Rosati, P., et al. 2023, A&A, 674, A79
Bertin, E. 2012, ASP Conf. Ser., 461, 263
Boldrin, M., Giocoli, C., Meneghetti, M., & Moscardini, L. 2012, MNRAS, 427, 3134
Boldrin, M., Giocoli, C., Meneghetti, M., et al. 2016, MNRAS, 457, 2738
Bouwens, R. J., Bradley, L., Zitrin, A., et al. 2014, ApJ, 795, 126
Bulbul, E., Liu, A., Kluge, M., et al. 2024, A&A, 685, A106
Caminha, G. B., Grillo, C., Rosati, P., et al. 2016, A&A, 587, A80
Caminha, G. B., Suyu, S. H., Grillo, C., & Rosati, P. 2022, A&A, 657, A83
Coe, D., Zitrin, A., Carrasco, M., et al. 2013, ApJ, 762, 32
Coe, D., Salmon, B., Bradač, M., et al. 2019, ApJ, 884, 85
Cuillandre, J.-C., Bertin, E., Bolzonella, M., et al. 2025, A&A, 697, A6
DESI Collaboration (Adame, A. G., et al.) 2024, AJ, 168, 58
Dey, A., Schlegel, D. J., Lang, D., et al. 2019, AJ, 157, 168
Diego, J. M., Meena, A. K., Adams, N. J., et al. 2023, A&A, 672, A3
Diego, J. M., Congedo, G., Gavazzi, R., et al. 2026, A&A, 706, A83
Ebeling, H., Edge, A. C., & Henry, J. P. 2001, ApJ, 553, 668
Ebeling, H., Richard, J., Beauchesne, B., et al. 2025, MNRAS, 537, 2662
Euclid Collaboration (Scaramella, R., et al.) 2022, A&A, 662, A112
Euclid Collaboration (Cropper, M., et al.) 2025, A&A, 697, A2
Euclid Collaboration (Jahnke, K., et al.) 2025, A&A, 697, A3
Euclid Collaboration (Mellier, Y., et al.) 2025, A&A, 697, A1
Euclid Collaboration (Aussel, H., et al.) 2026, A&A, 711, A1 (Euclid Q1 SI)
Euclid Collaboration (Bazzanini, L., et al.) 2026, A&A, in press, https://doi.org/10.1051/0004-6361/202557590
Euclid Collaboration (Bhargava, S., et al.) 2026, A&A, 711, A34 (Euclid Q1 SI)
Euclid Collaboration (Copin, Y., et al.) 2026, A&A, 711, A6 (Euclid Q1 SI)
Euclid Collaboration (Holloway, P., et al.) 2026, A&A, 711, A30 (Euclid Q1 SI)
Euclid Collaboration (Le Brun, V., et al.) 2026, A&A, 711, A7 (Euclid Q1 SI)
Euclid Collaboration (McCracken, H. J., et al.) 2026, A&A, 711, A2 (Euclid Q1 SI)
Euclid Collaboration (Polenta, G., et al.) 2026, A&A, 711, A3 (Euclid Q1 SI)
Euclid Collaboration (Romelli, E., et al.) 2026, A&A, 711, A4 (Euclid Q1 SI)
Euclid Collaboration (Tucci, M., et al.) 2025, A&A, 711, A5 (Euclid Q1 SI)
Euclid Collaboration (Walmsley, M., et al.) 2026, A&A, 711, A9 (Euclid Q1 SI)
Euclid Quick Release Q1 2025, https://doi.org/10.57780/esa-2853f3b
Furtak, L. J., Zitrin, A., Weaver, J. R., et al. 2023, MNRAS, 523, 4568
Gioia, I. M., Henry, J. P., Luppino, G. A., et al. 1995, A&A, 297, L75
Grillo, C., Suyu, S. H., Rosati, P., et al. 2015, ApJ, 800, 38
Grillo, C., Rosati, P., Suyu, S. H., et al. 2018, ApJ, 860, 94
Grillo, C., Pagano, L., Rosati, P., & Suyu, S. H. 2024, A&A, 684, L23
Guy, L. P., Cuillandre, J. C., Bachelet, E., et al. 2022, https://doi.org/10.5281/zenodo.5836022
Hashimoto, T., Laporte, N., Mawatari, K., et al. 2018, Nature, 557, 392
Hernández-Lang, D., Klein, M., Mohr, J. J., et al. 2023, MNRAS, 525, 24
Huchra, J. P., Macri, L. M., Masters, K. L., et al. 2012, ApJS, 199, 26
Jauzac, M., Eckert, D., Schwinn, J., et al. 2016, MNRAS, 463, 3876
Jullo, E., Natarajan, P., Kneib, J. P., et al. 2010, Science, 329, 924
Kelly, P. L., Rodney, S. A., Treu, T., et al. 2015, Science, 347, 1123
Kelly, P. L., Brammer, G., Selsing, J., et al. 2016, ApJ, 831, 205
Klein, M., Grandis, S., Mohr, J. J., et al. 2019, MNRAS, 488, 739
Klein, M., Hernández-Lang, D., Mohr, J. J., Bocquet, S., & Singh, A. 2023, MNRAS, 526, 3757
Klein, M., Mohr, J. J., Bocquet, S., et al. 2024a, MNRAS, 531, 3973
Klein, M., Mohr, J. J., & Davies, C. T. 2024b, A&A, 690, A322
Kluge, M., Comparat, J., Liu, A., et al. 2024, A&A, 688, A210
Koulouridis, E., Clerc, N., Sadibekova, T., et al. 2021, A&A, 652, A12
Laureijs, R., Amiaux, J., Arduini, S., et al. 2011, ArXiv e-prints [arXiv:1110.3193]
Liesenborgs, J., Williams, L. L. R., Wagner, J., & De Rijcke, S. 2020, MNRAS, 494, 3253
Magaña, J., Acebrón, A., Motta, V., et al. 2018, ApJ, 865, 122
Mahler, G., Richard, J., Clément, B., et al. 2018, MNRAS, 473, 663
Medezinski, E., Umetsu, K., Okabe, N., et al. 2016, ApJ, 817, 24
Melin, J. B., Bartlett, J. G., Tarrío, P., & Pratt, G. W. 2021, A&A, 647, A106
Meneghetti, M., Bartelmann, M., Dahle, H., & Limousin, M. 2013, Space Sci. Rev., 177, 31
Meneghetti, M., Davoli, G., Bergamini, P., et al. 2020, Science, 369, 1347
Meneghetti, M., Cui, W., Rasia, E., et al. 2023, A&A, 678, L2
Meštrić, U., Vanzella, E., Zanella, A., et al. 2022, MNRAS, 516, 3532
Niemiec, A., Jauzac, M., Eckert, D., et al. 2023, MNRAS, 524, 2883
Oguri, M. 2010, PASJ, 62, 1017

Oke, J. B. 1974, ApJS, 27, 21
Piffaretti, R., Arnaud, M., Pratt, G. W., Pointecouteau, E., & Melin, J. B. 2011, A&A, 534, A109
Rojas, K., Collett, T. E., Ballard, D., et al. 2023, MNRAS, 523, 4413
Rykoff, E. S., Rozo, E., Hollowood, D., et al. 2016, ApJS, 224, 1
Sadibekova, T., Arnaud, M., Pratt, G. W., Tarrío, P., & Melin, J. B. 2024, A&A, 688, A187
Schuldt, S., Cañameras, R., Andika, I. T., et al. 2025, A&A, 693, A291
Sharon, K., Bayliss, M. B., Dahle, H., et al. 2020, ApJS, 247, 12
Tarrío, P., Melin, J. B., & Arnaud, M. 2019, A&A, 626, A7
Umetsu, K., Sereno, M., Lieu, M., et al. 2020, ApJ, 890, 148
Vanzella, E., Loiacono, F., Messa, M., et al. 2024, A&A, 691, A251
Weaver, J., Taamoli, S., McPartland, C., et al. 2025, A&A, 697, A16
Wen, Z. L., & Han, J. L. 2024, ApJS, 272, 39
Wen, Z. L., Han, J. L., & Liu, F. S. 2012, ApJS, 199, 34
Wright, E. L., Eisenhardt, P. R. M., Mainzer, A. K., et al. 2010, AJ, 140, 1868

[1] Dipartimento di Fisica "Aldo Pontremoli", Università degli Studi di Milano, Via Celoria 16, 20133 Milano, Italy
[2] INAF-Osservatorio di Astrofisica e Scienza dello Spazio di Bologna, Via Piero Gobetti 93/3, 40129 Bologna, Italy
[3] INFN-Sezione di Bologna, Viale Berti Pichat 6/2, 40127, Bologna, Italy
[4] Instituto de Física de Cantabria, Edificio Juan Jordá, Avenida de los Castros, 39005 Santander, Spain
[5] Institute of Physics, Laboratory of Astrophysics, Ecole Polytechnique Fédérale de Lausanne (EPFL), Observatoire de Sauverny, 1290 Versoix, Switzerland
[6] SCITAS, Ecole Polytechnique Fédérale de Lausanne (EPFL), 1015 Lausanne, Switzerland
[7] INAF-IASF Milano, Via Alfonso Corti 12, 20133 Milano, Italy
[8] Dipartimento di Fisica e Scienze della Terra, Università degli Studi di Ferrara, Via Giuseppe Saragat 1, 44122 Ferrara, Italy
[9] INAF-Osservatorio Astronomico di Capodimonte, Via Moiariello 16, 80131 Napoli, Italy
[10] Institut de Recherche en Astrophysique et Planétologie (IRAP), Université de Toulouse, CNRS, UPS, CNES, 14 Av. Edouard Belin, 31400 Toulouse, France
[11] Minnesota Institute for Astrophysics, University of Minnesota, 116 Church St SE, Minneapolis, MN 55455, USA
[12] Kapteyn Astronomical Institute, University of Groningen, PO Box 800, 9700 AV Groningen, The Netherlands
[13] Department of Physics & Astronomy, University of California Irvine, Irvine, CA 92697, USA
[14] Dipartimento di Fisica e Astronomia "Augusto Righi" – Alma Mater Studiorum Università di Bologna, Via Piero Gobetti 93/2, 40129 Bologna, Italy
[15] Technical University of Munich, TUM School of Natural Sciences, Physics Department, James-Franck-Str. 1, 85748 Garching, Germany
[16] Max-Planck-Institut für Astrophysik, Karl-Schwarzschild-Str. 1, 85748 Garching, Germany
[17] Aix-Marseille Université, CNRS, CNES, LAM, Marseille, France
[18] Institut d'Astrophysique de Paris, UMR 7095, CNRS, and Sorbonne Université, 98 bis boulevard Arago, 75014 Paris, France
[19] Institute of Cosmology and Gravitation, University of Portsmouth, Portsmouth PO1 3FX, UK
[20] Laboratoire univers et particules de Montpellier, Université de Montpellier, CNRS, 34090 Montpellier, France
[21] Max-Planck-Institut für Astronomie, Königstuhl 17, 69117 Heidelberg, Germany
[22] STAR Institute, University of Liège, Quartier Agora, Allée du six Août 19c, 4000 Liège, Belgium
[23] Department of Physics, Centre for Extragalactic Astronomy, Durham University, South Road, Durham DH1 3LE, UK
[24] Department of Physics, Institute for Computational Cosmology, Durham University, South Road, Durham DH1 3LE, UK
[25] Departamento Física Aplicada, Universidad Politécnica de Cartagena, Campus Muralla del Mar, 30202 Cartagena, Murcia, Spain
[26] Center for Frontier Science, Chiba University, 1-33 Yayoi-cho, Inage-ku, Chiba 263-8522, Japan
[27] Department of Physics, Graduate School of Science, Chiba University, 1-33 Yayoi-Cho, Inage-Ku, Chiba 263-8522, Japan
[28] Dipartimento di Fisica e Astronomia, Università di Bologna, Via Gobetti 93/2, 40129 Bologna, Italy
[29] Centre de Recherche Astrophysique de Lyon, UMR5574, CNRS, Université Claude Bernard Lyon 1, ENS de Lyon, 69230 Saint-Genis-Laval, France
[30] University of Applied Sciences and Arts of Northwestern Switzerland, School of Engineering, 5210 Windisch, Switzerland
[31] Universitäts-Sternwarte München, Fakultät für Physik, Ludwig-Maximilians-Universität München, Scheinerstr. 1, 81679 München, Germany
[32] Max Planck Institute for Extraterrestrial Physics, Giessenbachstr. 1, 85748 Garching, Germany
[33] School of Physics and Astronomy, University of Birmingham, Birmingham B15 2TT, UK
[34] Department of Astrophysics, University of Vienna, Türkenschanzstrasse 17, 1180 Vienna, Austria
[35] Department of Physics and Astronomy, Lehman College of the CUNY, Bronx, NY 10468, USA
[36] American Museum of Natural History, Department of Astrophysics, New York, NY 10024, USA
[37] Caltech/IPAC, 1200 E. California Blvd., Pasadena, CA 91125, USA
[38] Institut de Ciències del Cosmos (ICCUB), Universitat de Barcelona (IEEC-UB), Martí i Franquès 1, 08028 Barcelona, Spain
[39] Shanghai Astronomical Observatory (SHAO), Nandan Road 80, Shanghai 200030, China
[40] Max Planck Institute for Gravitational Physics (Albert Einstein Institute), Am Muhlenberg 1, D-14476 Potsdam-Golm, Germany
[41] Université Paris-Saclay, CNRS, Institut d'Astrophysique Spatiale, 91405 Orsay, France
[42] ESAC/ESA, Camino Bajo del Castillo, s/n, Urb. Villafranca del Castillo, 28692 Villanueva de la Cañada, Madrid, Spain
[43] School of Mathematics and Physics, University of Surrey, Guildford, Surrey GU2 7XH, UK
[44] Institut für Theoretische Physik, University of Heidelberg, Philosophenweg 16, 69120 Heidelberg, Germany
[45] INAF-Osservatorio Astronomico di Brera, Via Brera 28, 20122 Milano, Italy
[46] Université Paris-Saclay, Université Paris Cité, CEA, CNRS, AIM, 91191 Gif-sur-Yvette, France
[47] IFPU, Institute for Fundamental Physics of the Universe, Via Beirut 2, 34151 Trieste, Italy
[48] INAF-Osservatorio Astronomico di Trieste, Via G. B. Tiepolo 11, 34143 Trieste, Italy
[49] INFN, Sezione di Trieste, Via Valerio 2, 34127 Trieste, TS, Italy
[50] SISSA, International School for Advanced Studies, Via Bonomea 265, 34136 Trieste, TS, Italy
[51] INAF-Osservatorio Astronomico di Padova, Via dell'Osservatorio 5, 35122 Padova, Italy
[52] Centre National d'Etudes Spatiales – Centre Spatial de Toulouse, 18 Avenue Edouard Belin, 31401 Toulouse Cedex 9, France
[53] Space Science Data Center, Italian Space Agency, Via del Politecnico snc, 00133 Roma, Italy
[54] INAF-Osservatorio Astrofisico di Torino, Via Osservatorio 20, 10025 Pino Torinese, (TO), Italy
[55] Dipartimento di Fisica, Università di Genova, Via Dodecaneso 33, 16146 Genova, Italy
[56] INFN-Sezione di Genova, Via Dodecaneso 33, 16146 Genova, Italy
[57] Department of Physics "E. Pancini", University Federico II, Via Cinthia 6, 80126 Napoli, Italy
[58] Instituto de Astrofísica e Ciências do Espaço, Universidade do Porto, CAUP, Rua das Estrelas, PT4150-762 Porto, Portugal
[59] Faculdade de Ciências da Universidade do Porto, Rua do Campo de Alegre, 4150-007 Porto, Portugal
[60] Dipartimento di Fisica, Università degli Studi di Torino, Via P. Giuria 1, 10125 Torino, Italy
[61] INFN-Sezione di Torino, Via P. Giuria 1, 10125 Torino, Italy

[62] European Space Agency/ESTEC, Keplerlaan 1, 2201 AZ Noordwijk, The Netherlands
[63] Institute Lorentz, Leiden University, Niels Bohrweg 2, 2333 CA Leiden, The Netherlands
[64] Leiden Observatory, Leiden University, Einsteinweg 55, 2333 CC Leiden, The Netherlands
[65] Centro de Investigaciones Energéticas, Medioambientales y Tecnológicas (CIEMAT), Avenida Complutense 40, 28040 Madrid, Spain
[66] Port d'Informació Científica, Campus UAB, C. Albareda s/n, 08193 Bellaterra, (Barcelona), Spain
[67] Institute for Theoretical Particle Physics and Cosmology (TTK), RWTH Aachen University, 52056 Aachen, Germany
[68] Institute of Space Sciences (ICE, CSIC), Campus UAB, Carrer de Can Magrans, s/n, 08193 Barcelona, Spain
[69] Institut d'Estudis Espacials de Catalunya (IEEC), Edifici RDIT, Campus UPC, 08860 Castelldefels, Barcelona, Spain
[70] INAF-Osservatorio Astronomico di Roma, Via Frascati 33, 00078 Monteporzio Catone, Italy
[71] INFN Section of Naples, Via Cinthia 6, 80126 Napoli, Italy
[72] Institute for Astronomy, University of Hawaii, 2680 Woodlawn Drive, Honolulu, HI 96822, USA
[73] Dipartimento di Fisica e Astronomia "Augusto Righi" – Alma Mater Studiorum Università di Bologna, Viale Berti Pichat 6/2, 40127 Bologna, Italy
[74] Instituto de Astrofísica de Canarias, E-38205 La Laguna, Tenerife, Spain
[75] Institute for Astronomy, University of Edinburgh, Royal Observatory, Blackford Hill, Edinburgh EH9 3HJ, UK
[76] Jodrell Bank Centre for Astrophysics, Department of Physics and Astronomy, University of Manchester, Oxford Road, Manchester M13 9PL, UK
[77] European Space Agency/ESRIN, Largo Galileo Galilei 1, 00044 Frascati, Roma, Italy
[78] Université Claude Bernard Lyon 1, CNRS/IN2P3, IP2I Lyon, UMR 5822, Villeurbanne F-69100, France
[79] Institució Catalana de Recerca i Estudis Avançats (ICREA), Passeig de Lluís Companys 23, 08010 Barcelona, Spain
[80] UCB Lyon 1, CNRS/IN2P3, IUF, IP2I Lyon, 4 Rue Enrico Fermi, 69622 Villeurbanne, France
[81] Mullard Space Science Laboratory, University College London, Holmbury St Mary, Dorking, Surrey RH5 6NT, UK
[82] Departamento de Física, Faculdade de Ciências, Universidade de Lisboa, Edifício C8, Campo Grande, PT1749-016 Lisboa, Portugal
[83] Instituto de Astrofísica e Ciências do Espaço, Faculdade de Ciências, Universidade de Lisboa, Campo Grande, 1749-016 Lisboa, Portugal
[84] Department of Astronomy, University of Geneva, Ch. d'Ecogia 16, 1290 Versoix, Switzerland
[85] INAF-Istituto di Astrofisica e Planetologia Spaziali, Via del Fosso del Cavaliere, 100, 00100 Roma, Italy
[86] INFN-Padova, Via Marzolo 8, 35131 Padova, Italy
[87] Aix-Marseille Université, CNRS/IN2P3, CPPM, Marseille, France
[88] INFN-Bologna, Via Irnerio 46, 40126 Bologna, Italy
[89] School of Physics, HH Wills Physics Laboratory, University of Bristol, Tyndall Avenue, Bristol BS8 1TL, UK
[90] FRACTAL S.L.N.E., calle Tulipán 2, Portal 13 1A, 28231 Las Rozas de Madrid, Spain
[91] INFN-Sezione di Milano, Via Celoria 16, 20133 Milano, Italy
[92] Institute of Theoretical Astrophysics, University of Oslo, P.O. Box 1029, Blindern 0315 Oslo, Norway
[93] Jet Propulsion Laboratory, California Institute of Technology, 4800 Oak Grove Drive, Pasadena, CA 91109, USA
[94] Felix Hormuth Engineering, Goethestr. 17, 69181 Leimen, Germany
[95] Technical University of Denmark, Elektrovej 327, 2800 Kgs. Lyngby, Denmark
[96] Cosmic Dawn Center (DAWN), Denmark
[97] NASA Goddard Space Flight Center, Greenbelt, MD 20771, USA
[98] Department of Physics and Astronomy, University College London, Gower Street, London WC1E 6BT, UK
[99] Department of Physics and Helsinki Institute of Physics, Gustaf Hällströmin katu 2, University of Helsinki, 00014 Helsinki, Finland
[100] Université de Genève, Département de Physique Théorique and Centre for Astroparticle Physics, 24 quai Ernest-Ansermet, CH-1211 Genève 4, Switzerland
[101] Department of Physics, P.O. Box 64, University of Helsinki, 00014 Helsinki, Finland
[102] Helsinki Institute of Physics, Gustaf Hällströmin katu 2, University of Helsinki, 00014 Helsinki, Finland
[103] Centre de Calcul de l'IN2P3/CNRS, 21 Avenue Pierre de Coubertin, 69627 Villeurbanne Cedex, France
[104] Laboratoire d'etude de l'Univers et des phenomenes eXtremes, Observatoire de Paris, Université PSL, Sorbonne Université, CNRS, 92190 Meudon, France
[105] SKAO, Jodrell Bank, Lower Withington, Macclesfield SK11 9FT, UK
[106] University of Applied Sciences and Arts of Northwestern Switzerland, School of Computer Science, 5210 Windisch, Switzerland
[107] Universität Bonn, Argelander-Institut für Astronomie, Auf dem Hügel 71, 53121 Bonn, Germany
[108] INFN-Sezione di Roma, Piazzale Aldo Moro, 2 – c/o Dipartimento di Fisica, Edificio G. Marconi, 00185 Roma, Italy
[109] Université Côte d'Azur, Observatoire de la Côte d'Azur, CNRS, Laboratoire Lagrange, Bd de l'Observatoire, CS 34229, 06304 Nice Cedex 4, France
[110] Université Paris Cité, CNRS, Astroparticule et Cosmologie, 75013 Paris, France
[111] CNRS-UCB International Research Laboratory, Centre Pierre Binétruy, IRL2007, CPB-IN2P3, Berkeley, USA
[112] Institut d'Astrophysique de Paris, 98bis Boulevard Arago, 75014 Paris, France
[113] Aurora Technology for European Space Agency (ESA), Camino bajo del Castillo s/n, Urbanizacion Villafranca del Castillo, Villanueva de la Cañada 28692, Madrid, Spain
[114] OCA, P.H.C Boulevard de l'Observatoire CS 34229, 06304 Nice Cedex 4, France
[115] Institut de Física d'Altes Energies (IFAE), The Barcelona Institute of Science and Technology, Campus UAB, 08193 Bellaterra, (Barcelona), Spain
[116] School of Mathematics, Statistics and Physics, Newcastle University, Herschel Building, Newcastle-upon-Tyne NE1 7RU, UK
[117] DARK, Niels Bohr Institute, University of Copenhagen, Jagtvej 155, 2200 Copenhagen, Denmark
[118] Waterloo Centre for Astrophysics, University of Waterloo, Waterloo, Ontario N2L 3G1, Canada
[119] Department of Physics and Astronomy, University of Waterloo, Waterloo, Ontario N2L 3G1, Canada
[120] Perimeter Institute for Theoretical Physics, Waterloo, Ontario N2L 2Y5, Canada
[121] Institute of Space Science, Str. Atomistilor, nr. 409 Măgurele, Ilfov 077125 Romania
[122] Consejo Superior de Investigaciones Cientificas, Calle Serrano 117, 28006 Madrid, Spain
[123] Universidad de La Laguna, Dpto. Astrofísica, E-38206 La Laguna, Tenerife, Spain
[124] Dipartimento di Fisica e Astronomia "G. Galilei", Università di Padova, Via Marzolo 8, 35131 Padova, Italy
[125] Université St Joseph; Faculty of Sciences, Beirut, Lebanon
[126] Departamento de Física, FCFM, Universidad de Chile, Blanco Encalada 2008, Santiago, Chile
[127] Satlantis, University Science Park, Sede Bld 48940, Leioa-Bilbao, Spain
[128] Department of Physics, Royal Holloway, University of London, Surrey TW20 0EX, UK
[129] Infrared Processing and Analysis Center, California Institute of Technology, Pasadena, CA 91125, USA

[130] Instituto de Astrofísica e Ciências do Espaço, Faculdade de Ciências, Universidade de Lisboa, Tapada da Ajuda, 1349-018 Lisboa, Portugal
[131] Cosmic Dawn Center (DAWN)
[132] Niels Bohr Institute, University of Copenhagen, Jagtvej 128, 2200 Copenhagen, Denmark
[133] Universidad Politécnica de Cartagena, Departamento de Electrónica y Tecnología de Computadoras, Plaza del Hospital 1, 30202 Cartagena, Spain
[134] Centre for Information Technology, University of Groningen, P.O. Box 11044, 9700 CA Groningen, The Netherlands
[135] Istituto Nazionale di Fisica Nucleare, Sezione di Ferrara, Via Giuseppe Saragat 1, 44122 Ferrara, Italy
[136] INAF, Istituto di Radioastronomia, Via Piero Gobetti 101, 40129 Bologna, Italy
[137] Department of Physics, Oxford University, Keble Road, Oxford OX1 3RH, UK
[138] Zentrum für Astronomie, Universität Heidelberg, Philosophenweg 12, 69120 Heidelberg, Germany
[139] Department of Mathematics and Physics E. De Giorgi, University of Salento, Via per Arnesano, CP-I93, 73100 Lecce, Italy
[140] INFN, Sezione di Lecce, Via per Arnesano, CP-193, 73100 Lecce, Italy
[141] INAF-Sezione di Lecce, c/o Dipartimento Matematica e Fisica, Via per Arnesano, 73100 Lecce, Italy
[142] INAF – Osservatorio Astronomico di Brera, Via Emilio Bianchi 46, 23807 Merate, Italy
[143] INAF-Osservatorio Astronomico di Brera, Via Brera 28, 20122 Milano, Italy, and INFN-Sezione di Genova, Via Dodecaneso 33, 16146 Genova, Italy
[144] ICL, Junia, Université Catholique de Lille, LITL, 59000 Lille, France
[145] ICSC – Centro Nazionale di Ricerca in High Performance Computing, Big Data e Quantum Computing, Via Magnanelli 2, Bologna, Italy
[146] Instituto de Física Teórica UAM-CSIC, Campus de Cantoblanco, 28049 Madrid, Spain
[147] CERCA/ISO, Department of Physics, Case Western Reserve University, 10900 Euclid Avenue, Cleveland OH 44106, USA
[148] Laboratoire Univers et Théorie, Observatoire de Paris, Université PSL, Université Paris Cité, CNRS, 92190 Meudon, France
[149] Departamento de Física Fundamental. Universidad de Salamanca, Plaza de la Merced s/n, 37008 Salamanca, Spain
[150] Université de Strasbourg, CNRS, Observatoire Astronomique de Strasbourg, UMR 7550, 67000 Strasbourg, France
[151] Center for Data-Driven Discovery, Kavli IPMU (WPI), UTIAS, The University of Tokyo, Kashiwa, Chiba 277-8583, Japan
[152] University Observatory, LMU Faculty of Physics, Scheinerstr. 1, 81679 Munich, Germany
[153] Max-Planck-Institut für Physik, Boltzmannstr. 8, 85748 Garching, Germany
[154] Dipartimento di Fisica – Sezione di Astronomia, Università di Trieste, Via Tiepolo 11, 34131 Trieste, Italy
[155] California Institute of Technology, 1200 E California Blvd, Pasadena, CA 91125, USA
[156] Instituto de Astrofísica de Canarias, E-38205 La Laguna; Universidad de La Laguna, Dpto. Astrofísica, E-38206 La Laguna, Tenerife, Spain
[157] CEA Saclay, DFR/IRFU, Service d'Astrophysique, Bat. 709, 91191 Gif-sur-Yvette, France
[158] Department of Astronomy, University of Florida, Bryant Space Science Center, Gainesville, FL 32611, USA
[159] Department of Computer Science, Aalto University, PO Box 15400, Espoo FI-00 076, Finland
[160] Ruhr University Bochum, Faculty of Physics and Astronomy, Astronomical Institute (AIRUB), German Centre for Cosmological Lensing (GCCL), 44780 Bochum, Germany
[161] Astrophysics Research Centre, University of KwaZulu-Natal, Westville Campus, Durban 4041, South Africa
[162] School of Mathematics, Statistics & Computer Science, University of KwaZulu-Natal, Westville Campus, Durban 4041, South Africa
[163] Department of Physics and Astronomy, Vesilinnantie 5, University of Turku, 20014 Turku, Finland
[164] Serco for European Space Agency (ESA), Camino bajo del Castillo, s/n, Urbanizacion Villafranca del Castillo, Villanueva de la Cañada 28692, Madrid, Spain
[165] ARC Centre of Excellence for Dark Matter Particle Physics, Melbourne, Australia
[166] Centre for Astrophysics & Supercomputing, Swinburne University of Technology, Hawthorn, Victoria 3122, Australia
[167] Department of Physics and Astronomy, University of the Western Cape, Bellville, Cape Town 7535, South Africa
[168] DAMTP, Centre for Mathematical Sciences, Wilberforce Road, Cambridge, CB3 0WA, UK
[169] Kavli Institute for Cosmology Cambridge, Madingley Road, Cambridge CB3 0HA, UK
[170] Department of Astrophysics, University of Zurich, Winterthurerstrasse 190, 8057 Zurich, Switzerland
[171] IRFU, CEA, Université Paris-Saclay, 91191 Gif-sur-Yvette Cedex, France
[172] Oskar Klein Centre for Cosmoparticle Physics, Department of Physics, Stockholm University, Stockholm SE-106 91, Sweden
[173] Astrophysics Group, Blackett Laboratory, Imperial College London, London SW7 2AZ, UK
[174] Univ. Grenoble Alpes, CNRS, Grenoble INP, LPSC-IN2P3, 53, Avenue des Martyrs, 38000 Grenoble, France
[175] INAF-Osservatorio Astrofisico di Arcetri, Largo E. Fermi 5, 50125 Firenze, Italy
[176] Dipartimento di Fisica, Sapienza Università di Roma, Piazzale Aldo Moro 2, 00185 Roma, Italy
[177] Centro de Astrofísica da Universidade do Porto, Rua das Estrelas, 4150-762 Porto, Portugal
[178] Dipartimento di Fisica, Università di Roma Tor Vergata, Via della Ricerca Scientifica 1, Roma, Italy
[179] INFN, Sezione di Roma 2, Via della Ricerca Scientifica 1, Roma, Italy
[180] HE Space for European Space Agency (ESA), Camino bajo del Castillo, s/n, Urbanizacion Villafranca del Castillo, Villanueva de la Cañada 28692, Madrid, Spain
[181] Department of Astrophysical Sciences, Peyton Hall, Princeton University, Princeton, NJ 08544, USA
[182] Theoretical astrophysics, Department of Physics and Astronomy, Uppsala University, Box 516, 751 37 Uppsala, Sweden
[183] Mathematical Institute, University of Leiden, Einsteinweg 55, 2333 CA Leiden, The Netherlands
[184] School of Physics & Astronomy, University of Southampton, Highfield Campus, Southampton SO17 1BJ, UK
[185] Institute of Astronomy, University of Cambridge, Madingley Road, Cambridge CB3 0HA, UK
[186] Department of Physics and Astronomy, University of California, Davis, CA 95616, USA
[187] Space physics and astronomy research unit, University of Oulu, Pentti Kaiteran katu 1, FI-90014 Oulu, Finland
[188] Center for Computational Astrophysics, Flatiron Institute, 162 5th Avenue, 10010 New York, NY, USA
[189] Department of Physics and Astronomy, University of British Columbia, Vancouver, BC V6T 1Z1, Canada

Appendix A: Lensing galaxy clusters identified in Phase 2

We present the catalogue of galaxy clusters visually inspected during Phase 2 and identified as strong gravitational lenses, with a lensing score $\mathcal{P}_{\rm lens} > 0.5$.

Table A.1. List of galaxy clusters in the Phase 2 run (VI catalogue) ranked with a score, $\mathcal{P}_{\rm lens}$, greater than 0.5 to be strong gravitational lenses.

Name	RA (J2000)	Dec (J2000)	$N_{\rm A}$	$N_{\rm B}$	$N_{\rm C}$	$\mathcal{P}_{\rm lens}$
ACT-CLJ0411.2−4819	62.80204	−48.31183	7	0	0	$1.00^{+0.00}_{-0.00}$
J174330.4+634142	265.87665	63.69491	7	0	0	$1.00^{+0.00}_{-0.00}$
ACT-CLJ0414.2−4612	63.55490	−46.20033	6	0	0	$1.00^{+0.00}_{-0.00}$
RMJ035713.8−475646.8	59.30752	−47.94633	6	0	0	$1.00^{+0.00}_{-0.00}$
J034919.5−485733	57.33133	−48.95924	6	0	0	$1.00^{+0.00}_{-0.00}$
J181749.7+651031	274.45724	65.17541	6	0	0	$1.00^{+0.00}_{-0.00}$
J181607.9+681651	274.03287	68.28094	6	0	0	$1.00^{+0.00}_{-0.00}$
J041810.0−491831	64.54186	−49.30865	6	0	0	$1.00^{+0.00}_{-0.00}$
J035312.7−502520	58.30281	−50.42233	7	0	0	$1.00^{+0.00}_{-0.00}$
J033326.3−295130	53.35960	−29.85820	7	0	0	$1.00^{+0.00}_{-0.00}$
RMJ040125.7−475359.1	60.35721	−47.89974	7	0	0	$1.00^{+0.00}_{-0.00}$
J033459.3−263432	53.74707	−26.57546	7	0	0	$1.00^{+0.00}_{-0.00}$
J032818.9−291447	52.07892	−29.24641	7	0	0	$1.00^{+0.00}_{-0.00}$
J040359.6−460654	60.99849	−46.11512	6	1	0	$0.93^{+0.07}_{-0.07}$
J033045.3−292954	52.68888	−29.49828	6	1	0	$0.93^{+0.07}_{-0.07}$
MARDJ035850.4−500844	59.71026	−50.14557	5	1	0	$0.92^{+0.08}_{-0.09}$
RMJ040205.1−480808.6	60.52128	−48.13571	5	1	0	$0.92^{+0.08}_{-0.09}$
J032331.2−273855	50.87982	−27.64863	5	1	0	$0.92^{+0.08}_{-0.09}$
J041128.4−454223	62.86826	−45.70646	5	1	0	$0.92^{+0.08}_{-0.09}$
J033103.6−264803	52.76483	−26.80084	5	1	0	$0.92^{+0.08}_{-0.09}$
J034824.7−503740	57.10284	−50.62782	4	1	0	$0.90^{+0.10}_{-0.10}$
ACT-CLJ0405.9−4915★†	61.49234	−49.26265	5	2	0	$0.86^{+0.07}_{-0.07}$
J035934.0−493634	59.89167	−49.60939	6	0	1	$0.86^{+0.14}_{-0.15}$
RMJ033747.0−275109.1	54.44571	−27.85253	6	0	1	$0.86^{+0.14}_{-0.15}$
RMJ040202.3−483429.6	60.50947	−48.57489	6	0	1	$0.86^{+0.14}_{-0.15}$
J040700.7−495324	61.75287	−49.88997	6	0	1	$0.86^{+0.14}_{-0.15}$
1eRASSJ040349.4−501834	60.95596	−50.30948	4	2	0	$0.83^{+0.09}_{-0.08}$
ACT-CLJ0406.8−4804★	61.72112	−48.08194	4	2	0	$0.83^{+0.09}_{-0.08}$
J032308.0−275431	50.78328	−27.90866	3	2	0	$0.80^{+0.10}_{-0.10}$
J033036.3−294946	52.65122	−29.82954	5	1	1	$0.79^{+0.14}_{-0.15}$
J033017.5−270214	52.57312	−27.03715	5	1	1	$0.79^{+0.14}_{-0.15}$
ACT-CLJ0348.7−4902	57.19855	−49.03517	4	3	0	$0.79^{+0.07}_{-0.08}$
WH-J180447.7+645009	271.19867	64.83583	5	1	1	$0.79^{+0.14}_{-0.15}$
J041017.3−471205	62.57214	−47.20138	4	3	0	$0.79^{+0.07}_{-0.08}$
J033509.5−271544	53.78942	−27.26222	4	3	0	$0.79^{+0.07}_{-0.08}$
J174145.3+650415	265.43884	65.07072	4	3	0	$0.79^{+0.07}_{-0.08}$
J175226.0+640222	268.10834	64.03943	3	3	0	$0.75^{+0.08}_{-0.08}$
J035155.7−505110	57.98199	−50.85278	3	3	0	$0.75^{+0.08}_{-0.08}$

Table A.1. Continued.

Name	RA (J2000)	Dec (J2000)	N_A	N_B	N_C	$\mathcal{P}_{lens}$
ACT-CLJ0417.3−4748	64.36486	−47.80644	3	3	0	$0.75^{+0.08}_{-0.08}$
RMJ042030.7−471830.3	65.12794	−47.30842	2	2	0	$0.75^{+0.12}_{-0.12}$
J180154.6+655505	270.47757	65.91805	4	1	1	$0.75^{+0.17}_{-0.17}$
J033914.1−284018	54.80862	−28.67169	5	0	2	$0.71^{+0.15}_{-0.14}$
RMJ033906.2−283952.0	54.77564	−28.66445	5	0	2	$0.71^{+0.15}_{-0.14}$
RMJ033859.1−281343.8	54.74643	−28.22884	4	2	1	$0.71^{+0.15}_{-0.14}$
RMJ042202.1−473203.4	65.50886	−47.53427	4	2	1	$0.71^{+0.15}_{-0.14}$
J032552.8−263516	51.47007	−26.58788	3	4	0	$0.71^{+0.08}_{-0.07}$
1eRASSJ040508.4−464833	61.28504	−46.80940	4	2	1	$0.71^{+0.15}_{-0.14}$
RASS-CLJ175517+6416.4	268.82240	64.27478	2	3	0	$0.70^{+0.10}_{-0.10}$
J180413.7+655051	271.05707	65.84746	2	4	0	$0.67^{+0.08}_{-0.09}$
J041927.4−461501	64.86410	−46.25023	2	4	0	$0.67^{+0.08}_{-0.09}$
J032908.6−284850	52.28573	−28.81401	2	4	0	$0.67^{+0.08}_{-0.09}$
J032822.0−264946	52.09173	−26.82952	3	2	1	$0.67^{+0.16}_{-0.17}$
J181756.0+654013	274.48322	65.67028	2	4	0	$0.67^{+0.08}_{-0.09}$
J034007.3−285039	55.03021	−28.84417	3	2	1	$0.67^{+0.16}_{-0.17}$
J032318.6−273811	50.82745	−27.63629	2	4	0	$0.67^{+0.08}_{-0.09}$
ACO2281	265.75434	64.64593	2	5	0	$0.64^{+0.07}_{-0.07}$
ACT-CLJ0408.6−4936	62.17195	−49.60805	3	3	1	$0.64^{+0.15}_{-0.14}$
J040311.3−485049	60.79692	−48.84685	3	3	1	$0.64^{+0.15}_{-0.14}$
RMJ035309.8−473758.4	58.29069	−47.63289	3	3	1	$0.64^{+0.15}_{-0.14}$
J032404.4−274649	51.01817	−27.78036	3	3	1	$0.64^{+0.15}_{-0.14}$
J035104.8−505605	57.77018	−50.93467	1	4	0	$0.60^{+0.10}_{-0.10}$
RMJ035053.0−490551.9	57.72087	−49.09774	1	4	0	$0.60^{+0.10}_{-0.10}$
J033219.7−261535	53.08212	−26.25968	1	4	0	$0.60^{+0.10}_{-0.10}$
J040049.6−491016	60.20680	−49.17115	1	4	0	$0.60^{+0.10}_{-0.10}$
J174744.3+652823	266.93460	65.47315	1	4	0	$0.60^{+0.10}_{-0.10}$
J032443.9−282129★	51.18295	−28.35814	2	3	1	$0.58^{+0.17}_{-0.16}$
J033026.2−281711	52.60900	−28.28640	2	3	1	$0.58^{+0.17}_{-0.16}$
1eRASSJ034629.0−493512	56.62101	−49.58693	2	3	1	$0.58^{+0.17}_{-0.16}$
ACT-CLJ0349.1−4741	57.29851	−47.69243	1	5	0	$0.58^{+0.09}_{-0.08}$
J032520.8−274334	51.33658	−27.72617	1	5	0	$0.58^{+0.09}_{-0.08}$
J180437.0+662706	271.15417	66.45170	2	4	1	$0.57^{+0.14}_{-0.14}$
J180746.5+664844	271.94370	66.81219	1	6	0	$0.57^{+0.07}_{-0.07}$
J033521.5−293641	53.83970	−29.61131	3	2	2	$0.57^{+0.14}_{-0.14}$
RXJ1745.2+6556	266.31750	65.93810	4	0	3	$0.57^{+0.14}_{-0.14}$
RMJ041113.1−491024.9	62.80475	−49.17359	1	6	0	$0.57^{+0.07}_{-0.07}$
J033552.4−262805	53.96844	−26.46815	2	5	1	$0.56^{+0.13}_{-0.12}$

Notes. For each galaxy cluster, we report the number of A, B, and C votes (N_A, N_B, and N_C) assigned by the inspectors. The uncertainty associated with the lensing score is computed as described in Sect. 4. The star (★) and dagger (†) symbols mark the gravitational lenses previously observed by the *Hubble* Space Telescope and *James Webb* Space Telescope, respectively.